

Relating spatially resolved optical attenuation, dust, and gas in nearby galaxies

E. D. Paspaliaris^{1,*}, S. Bianchi¹, E. Corbelli¹, and A. Concas^{2,3}

¹ INAF – Osservatorio Astrofisico di Arcetri, Largo E. Fermi 5, 50125 Florence, Italy

² European Southern Observatory, Karl-Schwarzschild-Strasse 2, 85748 Garching bei München, Germany

³ Scuola Normale Superiore, Piazza dei Cavalieri 7, 50126 Pisa, Italy

Received 11 April 2025 / Accepted 15 August 2025

ABSTRACT

Aims. The purpose of the present study is to relate the optical attenuation inferred by the Balmer decrement, $A_{V,BD}$, and by the spectral energy distribution (SED) fitting, $A_{V,SED}$, to the dust distribution and gas surface density throughout the disc of galaxies, down to scales smaller than 0.5 kpc.

Methods. We investigated five nearby *Herschel*-detected star-forming spiral galaxies with available far-ultraviolet to sub-millimetre observations, along with atomic and molecular gas surface density maps and optical integral-field spectroscopic data. We used the CIGALE SED-fitting code to map the dust mass surface density (Σ_{dust}) and $A_{V,SED}$ of different stellar populations. For each pixel, we independently estimated the attenuation from the Balmer decrement.

Results. We find that both Σ_{dust} and $A_{V,BD}$ are better at tracing the molecular and total gas mass surface density than the atomic gas. Since regions sampled in this study have high molecular fractions, atomic gas surface densities, indicative of molecular gas shielding layers, decrease as the mean dust-to-gas ratio increases from galaxy to galaxy. The fitted attenuation towards the young stellar population, $A_{V,SED}^{young}$, is in good agreement with $A_{V,BD}$. It can then be used to trace the attenuation in star-forming galaxies for which integral-field observations are not available. We estimate the ratio of $A_{V,BD}$ over the total stellar $A_{V,SED}$ and find it slightly larger than what has been found in previous studies. Finally, we investigate which dust distribution better reproduces the estimated $A_{V,BD}$ and $A_{V,SED}$. We find that the attenuation towards old stars is consistent with the expectations for a standard galactic disc, where the stellar and dust distributions are mixed, while $A_{V,BD}$ and $A_{V,SED}^{young}$ are between the values expected for a foreground dust screen and the mixed configuration.

Key words. ISM: abundances – ISM: atoms – dust, extinction – ISM: molecules – galaxies: ISM – galaxies: spiral

1. Introduction

Dust is a crucial component of the interstellar medium (ISM) and plays a significant role in regulating the rate at which stars are formed, and hence galaxy evolution. Dust grains catalyse the transformation of atomic gas into molecular gas, which can cool and fragment forming stars under the power of gravity. Radiation from massive stars heats the gas but it is also absorbed by dust both locally, and in the diffuse ISM. The ultimate goal of understanding what drives star formation across a variety of galaxy discs, and consequently their evolution, can thus be achieved only by understanding the complex interplay among the various galaxy building blocks, such as cold, warm and hot ISM phases, interstellar dust, and stellar populations.

However, tracing the three main components of the ISM (atomic gas, molecules, and dust) is not a simple task. The 21 cm line traces the atomic hydrogen gas well but it is challenging to detect individual galaxies at $z > 0.3$ with current facilities (Catinella et al. 2008; Verheijen et al. 2010). In contrast, CO lines can be observed up to intermediate redshifts, but they do not trace the dominant component of the molecular gas (H_2) and a conversion factor between the two is needed. Direct estimates of total gas mass of unresolved high- z galaxies are often not

available or limited to the bright ones, because millimetre/radio spectroscopy is more time-consuming than optical spectroscopy. To overcome this limitation, optical spectra have been used to estimate gas masses (Brinchmann et al. 2013). Furthermore, the far-infrared (FIR) dust emission or the optical attenuation (A_V) inferred from SED fitting ($A_{V,SED}$) or from the Balmer decrement (BD, the ratio $F_{H\alpha}/F_{H\beta}$, usually converted to a dust attenuation $A_{V,BD}$), have been used to trace the gas mass. A few studies have specifically explored how HI and CO line emission correlate with dust and A_V , and how dust emission correlates with A_V .

The literature does not yet provide a consistent picture of which gas phase shows a stronger correlation with dust. Despite it being clearer that the atomic gas has a loose correlation with the dust, it is still uncertain if dust traces the molecular gas or the total gas better. Those relations have been examined for various galaxy samples, on both global (e.g. Corbelli et al. 2012; Grossi et al. 2016; Orellana et al. 2017; Casasola et al. 2020; Salvestrini et al. 2025) and resolved scales (e.g. Abdurro'uf et al. 2022; Casasola et al. 2022). Corbelli et al. (2012) studied 35 metal-rich galaxies in the Virgo Cluster and found that the dust mass correlates better with the total gas mass surface density (Σ_{gas}) than with the atomic (Σ_{HI}) or molecular surface density (Σ_{H_2}). The latter result is confirmed by Orellana et al. (2017), for 1630 ($z < 0.1$) galaxies, and Casasola et al. (2020), for a sample of 252 DustPedia late-type galaxies. For resolved galaxies such as NGC 5236 and

* Corresponding author: evangelos.paspaliaris@inaf.it, edpaspaliaris@gmail.com

Table 1. Galaxies in our sample and their integrated properties.

ID	RA	Dec	Type	D ₂₅	D	pw	<i>i</i>	PA	M_{HI}	M_{H_2}	SFR	M_{star}	M_{dust}
(1)	[h:min:sec (2)]	[°:′:″ (3)]	(4)	[arcmin] (5)	[Mpc] (6)	[kpc] (7)	[°] (8)	[°] (9)	[10 ⁹ M _⊙] (10)	[10 ⁹ M _⊙] (11)	[M _⊙ yr ⁻¹] (12)	[10 ⁹ M _⊙] (13)	[10 ⁷ M _⊙] (14)
NGC 0628	01:36:41.745	+15:47:1.11	Sc	10.00	9.84	0.29	19.8	20	3.8	1.0	2.4±0.5	14.1±0.2	3.8±1.2
NGC 3351	10:43:57.700	+11:42:13.70	SBb	7.24	9.96	0.29	54.6	192	1.2	1.0	1.1±0.2	27.4±0.6	0.8±0.1
NGC 3627	11:20:14.964	+12:59:29.54	SABb	10.23	11.32	0.33	67.5	173	0.82	1.3	3.0±1.0	67.0±11.7	2.8±0.2
NGC 4254	12:18:49.604	+14:24:59.43	Sc	5.01	13.10	0.38	20.1	68	4.4	26.3	5.2±0.5	13.4±0.2	2.2±0.1
NGC 4321	12:22:54.831	+15:49:18.54	SABb	6.17	15.21	0.44	23.4	30	2.9	20.9	6.0±1.2	49.5±1.1	3.7±0.4

Notes. (1) NGC number; (2) and (3) J2000 right ascension and declination; (4) Hubble type; (5) major axis of the optical 25 mag arcsec⁻² isophote; (6) distance (Anand et al. 2021); (7) pixel width in physical scale; (8) inclination; (9) Position Angle (Walter et al. 2008; Chung et al. 2009); (10) total atomic gas mass (Walter et al. 2008; Chung et al. 2009); (11) total molecular gas mass (Leroy et al. 2008; Draine et al. 2007); (12) global SFR; (13) total stellar mass; (14) total dust mass. When no reference is indicated, data is from the DustPedia archive.

NGC 0891, Foyle et al. (2012) and Hughes et al. (2014) found a weak correlation between Σ_{dust} and Σ_{HI} , and a similarly tight relation between $\Sigma_{\text{dust}}-\Sigma_{\text{H}_2}$ and $\Sigma_{\text{dust}}-\Sigma_{\text{gas}}$. This picture is confirmed by Casasola et al. (2022), for a sample of 18 DustPedia galaxies at resolved (kiloparsec and sub-kiloparsec) scales. Also, Abdurro’uf et al. (2022) for a sample of ten nearby galaxies (including four out of the five galaxies studied in this work) recover a tighter and more significant correlation for $\Sigma_{\text{dust}}-\Sigma_{\text{gas}}$, rather than for $\Sigma_{\text{dust}}-\Sigma_{\text{H}_2}$, while for the $\Sigma_{\text{dust}}-\Sigma_{\text{HI}}$ relation the scatter increases and the correlation is moderate.

With respect to the relationship between the gas and A_V , for a sample of 222 local unresolved star-forming galaxies from the xCold GASS survey, Concas & Popesso (2019) find that the BD can be a powerful proxy of the molecular gas with a scatter of ~ 0.3 dex, after correcting for disc inclination. They also find that the BD is not correlated with the HI gas, while its correlation with the total gas is modest. The use of integrated quantities limits our understanding of what drives the correlation, however, and leaves open the question of the role of the HI gas, which is more extended than the star-forming disc and hard to estimate within the area traced by the BD if galaxies are unresolved. Barrera-Ballesteros et al. (2020) find a tight correlation of the BD with the Σ_{gas} , though they only use a low universal value for Σ_{HI} . In that study they also find that although the scatter increases as smaller scales are sampled, the overall $\Sigma_{\text{dust}}-\Sigma_{\text{gas}}$ relation does not significantly depend on the scale. However, the question of whether the correlation of the BD with HI or total gas is tighter than with the CO alone remains uncertain. On kiloparsec scales, Concas et al. (in preparation) analyse ALMAQUEST data and find a clear correlation between $A_{V,\text{BD}}$ and Σ_{H_2} (derived from CO(1-0) observations), with a significantly smaller dispersion than the one found by Barrera-Ballesteros et al. (2020). Using the A_{FUV} , for a sample of 4 resolved and 27 unresolved galaxies, Boquien et al. (2013) found little correlation of the attenuation with the Σ_{HI} , and a good correlation with Σ_{H_2} and Σ_{gas} .

Regarding the correlation between Σ_{dust} and the BD, Farley et al. (2025) examine how it varies on global scales, assuming several dust geometries and using a large sample from the Galaxy and Mass Assembly (GAMA) survey. In a study based on eight spatially resolved nearby galaxies, Kreckel et al. (2013) found a correlation between Σ_{dust} and $A_{V,\text{BD}}$; however, they cautioned against using the BD to infer dust properties globally.

In the current study, for the first time, we make a full comparison of the dust surface density, Σ_{dust} , the surface density of all gas components, Σ_{HI} , Σ_{H_2} , and Σ_{gas} , and the optical attenuation derived from both BD, $A_{V,\text{BD}}$, and SED fitting, $A_{V,\text{SED}}$, relative to a sample of five nearby spiral galaxies observed with good

spatial resolution. To achieve this, we perform a pixel-by-pixel SED-fitting analysis to derive their physical properties (e.g. Σ_{dust} and $A_{V,\text{SED}}$) in the lowest possible resolved scale. We create maps of the $A_{V,\text{BD}}$ and Σ_{gas} , extracted from H α , H β and CO, HI maps, respectively. In Section 2 we present the data, the data processing steps, and our methodology. Results are discussed in Section 3. Finally, our findings are summarised in Section 4. In Appendix A we show spatially resolved maps of several physical quantities used or derived for each galaxy in the sample. In Appendix B we discuss possible variations in the CO-to-H₂ conversion factor and of the ¹²CO J = 2-1/J = 1-0 line ratio. In Appendix C we present how attenuations are computed for simple geometries.

2. Sample, data, and processing

The main aim of our project is to examine a sample of large and well-resolved local spiral galaxies with atomic and molecular gas maps, integral-field optical spectra, and dust emission data, available throughout the star-forming disc. We selected all the nearby galaxies with the aforementioned observational data, which also have low or moderate inclinations ($i < 70^\circ$) to avoid overestimating the A_V (Concas & Popesso 2019). The five selected galaxies are NGC 0628, NGC 3351, NGC 3627, NGC 4254, and NGC 4321. Detailed information about the integrated properties of our targets are shown in Table 1.

We used data from the DustPedia research project¹ which includes far-ultraviolet (FUV) to sub-millimetre observations of 875 nearby galaxies that lie within 40 Mpc distance and have an optical diameter larger than 1 arcmin. All DustPedia galaxies are observed by the *Herschel* Space Observatory (Pilbratt et al. 2010), which helps constrain their dust content. For more information on the DustPedia project, we refer the reader to Davies et al. (2019) and Clark et al. (2018).

2.1. The data

To perform a spatially resolved analysis of the relation between the dust attenuation and the gas surface density, down to a sub-kiloparsec physical scale (which corresponds to the pixel size of SPIRE-250 μm image), we processed the data following specific steps in order to create a homogeneous dataset with common resolution and pixel scale across all wavebands. The pixel width of each galaxy, in physical units, is listed in Table 1. The multi-wavelength data used in the current study are listed in Table 2. Below we describe the data processing.

¹ <http://dustpedia.astro.noa.gr>

Table 2. Summary of the multi-wavelength observational data used in the current analysis with their references.

Survey/Telescope	Band name (effective wavelength; λ)
VLT-MUSE ^a	H β (4861 Å)
VLT-MUSE ^a	H α (6562 Å)
GALEX ^b	FUV (153 nm), NUV (227 nm)
SDSS ^c	u (353 nm), g (475 nm), r (622 nm), i (763 nm), z (905 nm)
2MASS ^d	J (1.24 μ m), H (1.66 μ m), Ks (2.16 μ m)
WISE ^e	W1 (3.4 μ m), W2 (4.6 μ m), W3 (12 μ m), W4 (22 μ m)
SPITZER ^f	IRAC ^g (3.6 μ m, 4.5 μ m, 8.0 μ m, 12 μ m), MIPS ^h (24 μ m)
HERSCHEL ⁱ	PACS ^j (70 μ m, 100 μ m, 160 μ m), SPIRE ^k (250 μ m)
HERACLES ^l	¹² CO(2-1) (1.3 mm)
THINGS ^m /VIVA ⁿ	HI (21 cm)

Notes. ^aEmsellem et al. (2022); ^bMartin et al. (2005), Morrissey et al. (2007); ^cYork et al. (2000), Eisenstein et al. (2011); ^dSkrutskie et al. (2006); ^eWright et al. (2010); ^fWerner et al. (2004); ^gFazio et al. (2004); ^hRieke et al. (2004); ⁱPilbratt et al. (2010); ^jPoglitsch et al. (2010); ^kGriffin et al. (2010); ^lLeroy et al. (2009); ^mWalter et al. (2008); ⁿChung et al. (2009).

2.1.1. Galaxy images from FUV to FIR bands

We selected DustPedia images from FUV to 250 μ m emission and processed them following the steps described hereafter.

- (i) We first removed foreground stars in the field of view of images up to the NIR, using the Cutri et al. (2003) 2MASS all-sky catalogue of point sources. To optimally remove a foreground star, we assumed that the area to be removed depends on the brightness of the star and on the spatial resolution (FWHM) of the image.
- (ii) Fluxes in bands shorter than 10 μ m were corrected for foreground galactic extinction, following the same methodology presented in Clark et al. (2018). We assume $R_V = 3.1$ with a Cardelli et al. (1989) extinction curve. The A_λ over $E(B - V)$ ratio is taken from Gil de Paz et al. (2007) for the FUV and NUV bands and from Schlafly & Finkbeiner (2011) for the other bands (see the IRSA Dust Extinction Service²).
- (iii) We convolved the data to the point spread function (PSF) of the band with the poorest resolution, which is the SPIRE-250 μ m band (18''). We used the Aniano et al. (2011) set of convolution kernels to degrade the resolution of all the shorter bands to the SPIRE-250 μ m PSF. In Sect. 2.3 we comment on the impact of neglecting the longest wavelength (and poorest resolution) SPIRE bands.
- (iv) After convolving the images, we used IRAF (Tody 1986, 1993) to create a reference frame for each band, centred on the coordinates of the galaxy centre in the SPIRE-250 μ m image. We also selected the pixel size of the reference frame to be equal to the pixel size of SPIRE-250 μ m band (6'') and the creation of the reference frame was done with the MKPATTERN package. Using the WREGISTER package, we registered all images on the reference frame and we ended up having aligned images from different telescopes with a common PSF and pixel scale.
- (v) Once we had all images on the same grid, we subtracted the background noise. To successfully subtract inhomogeneities of the background, such as moiré patterns

(GALEX, SDSS), foreground emission (e.g. sky brightness in NIR, Galactic cirrus in MIR and FIR), instrumental gradient (common in GALEX and Spitzer bands), which could affect our results, we modelled the complex sky with the Background2D class of the Photutils package in AstroPy.

- (vi) Finally, pixels with low signal-to-noise ratio (S/N), which consequently do not have a clear physical connection with the galaxy, were discarded by applying a 3- σ cut to the images. After applying the pixel filtering, we took into consideration in our SED-fitting analysis only those pixels featuring at least 11 bands above 3- σ , providing that SPIRE-250 μ m and at least one more *Herschel* band are included. The flux uncertainty of each pixel is estimated as the quadrature sum of the standard deviation of the flux in an annulus around the galaxy and the photometric calibration uncertainty of each band. The calibration uncertainties are taken from Clark et al. (2018). We manually added an additional source of error, equal to 10% of the flux, to account for uncertainties in the models used in the SED-fitting modelling as well as for unknown systematic errors in the photometry, as suggested by Noll et al. (2009) and as it is typically done in previous analyses (e.g. Nersesian et al. 2019; Paspaliaris et al. 2021, 2023, among others).

2.1.2. Gas mass surface density maps

To trace the atomic and molecular gas content of the galaxies, we used HI 21 cm and ¹²CO(2-1) line emission maps, respectively. The 21 cm line emission maps (“moment 0”; in Jy beam⁻¹ m s⁻¹) are drawn from “The HI Nearby Galaxy Survey” (THINGS; Walter et al. 2008) for NGC 0628, NGC 3351 and NGC 3627, and the “VLA Imaging of Virgo in Atomic Gas” (VIVA; Chung et al. 2009) survey for NGC 4254 and NGC 4321. THINGS is undertaken at Very Large Array (VLA) of the National Radio Astronomy Observatory program that performed 21 cm HI observations of 34 nearby galaxies. We used the ROBUST dataset, providing a close to uniform synthesised beam with FWHM \approx 6'' across the image. VIVA is an HI imaging survey of 53 late-type Virgo cluster galaxies, at a resolution of 15''. The ¹²CO(2-1) line integrated intensity maps (in K km s⁻¹) are taken from “The HERA CO-Line Extragalactic Survey” (HERACLES; Leroy et al. 2009). HERACLES provides ¹²CO(2-1) emission maps of 48 nearby galaxies, observed with the IRAM-30 m telescope, at a resolution of 13.4''.

The PHANGS-ALMA survey (Leroy et al. 2021) provides high-quality CO(2-1) maps of 90 nearby galaxies, including the ones that we study in the current work. However, due to the limited field-of-view for each galaxy, we prefer to use the HERACLES maps. It has been reported that the HERACLES CO(2-1) map of NGC 3627 might suffer from calibration issues (see, den Brok et al. 2021; Leroy et al. 2021). In a recent study, however, Kovačić et al. (2025) compare this map with a more recent ALMA map and find only minor differences, of the order of $0.06^{+0.11}_{-0.26}$ dex.

The integrated HI and CO maps were convolved, re-gridded, and 3- σ filtered (see, Walter et al. 2008; Chung et al. 2009; Leroy et al. 2009, or detailed information on the data processing of THINGS, VIVA and HERACLES data, respectively). We assumed that their original PSF is a Gaussian of the corresponding size. To perform the 3- σ filtering, in THINGS maps we used the robust noise in one channel map, provided in Table 2 of Walter et al. (2008), while a flux calibration uncertainty of the order of 5% dominates the measurements of the flux densities. In the case of VIVA maps, we adopted the root mean square (rms)

² <https://irsa.ipac.caltech.edu/applications/DUST/>

values measured by [Chung et al. \(2009\)](#) (see their Table 2) using the areas outside of the HI emission. For the HERACLES maps of NGC 0628 and NGC 3351, we used the rms intensity level provided by [Leroy et al. \(2009\)](#) (see their Table 3). For the other galaxies we estimated the rms using the areas outside the CO emission in the convolved and re-gridded moment-zero error-maps. We then used the 3- σ filtered maps to derive gas mass surface density maps.

The atomic gas mass surface density, Σ_{HI} , was calculated under the assumption of optically thin emission using the HI 21 cm line intensity maps as

$$\Sigma_{\text{HI}} [\text{M}_{\odot} \text{pc}^{-2}] = 0.020 I_{21 \text{ cm}} [\text{K km s}^{-1}], \quad (1)$$

where the HI column density has been multiplied by a factor 1.36 to account for heavy elements ([Leroy et al. 2012](#)). The maps were converted from units of [$\text{Jy beam}^{-1} \text{m s}^{-1}$] to antenna temperature [K km s^{-1}] using Eq. (1) of [Walter et al. \(2008\)](#) and the synthesised beam size given in their Table 2 for THINGS galaxies, and in Table 2 of [Chung et al. \(2009\)](#) for VIVA galaxies.

The surface density of the molecular gas mass, Σ_{H_2} , was derived using the $^{12}\text{CO}(2-1)$ line brightness, via the following equation ([Leroy et al. 2012](#)):

$$\Sigma_{\text{H}_2} [\text{M}_{\odot} \text{pc}^{-2}] = 6.3 I_{\text{CO}} [\text{K km s}^{-1}], \quad (2)$$

which assumes a CO(2-1)-to-CO(1-0) line ratio $R_{21} = 0.7$ (see e.g. [Leroy et al. 2009](#); [Schruba et al. 2011](#)) and a Milky Way (MW) CO-to-H₂ conversion factor of $\alpha_{\text{CO}} = 4.4 \text{M}_{\odot} \text{pc}^{-2} (\text{K km s}^{-1})^{-1}$ ([Bolatto et al. 2013](#)) that corresponds to $X_{\text{CO}} = 2 \times 10^{20} \text{cm}^{-2} (\text{K km s}^{-1})^{-1}$ and includes the correction for heavy elements. The assumed α_{CO} is an intermediate value among those determined by various studies (e.g. [Strong & Mattox 1996](#); [Dame et al. 2001](#); [Abdo et al. 2010](#); [Shetty et al. 2011](#)). This specific α_{CO} value is found to be optimal when investigating nearby spiral galaxies with metallicities close to solar (e.g. [Wong & Blitz 2002](#); [Leroy et al. 2008](#)), such as our targets. Both R_{21} and α_{CO} are assumed to be constant throughout galaxy discs unless stated differently. Possible variations in α_{CO} and R_{21} are discussed in Appendix B. The total gas mass surface density, Σ_{gas} , is the sum of Σ_{HI} and Σ_{H_2} .

2.2. Dust-attenuation maps from Balmer decrement

With the aim of estimating the dust absorption from the BD, we used data from the PHANGS-MUSE survey ([Emsellem et al. 2022](#)). PHANGS-MUSE used the MUSE integral field spectrograph at the VLT to map 19 star-forming disc galaxies, at a resolution lower than 1". For each galaxy, spectral cubes were created by mosaicking several pointings (up to 15) and convolving the final frames to a common angular resolution ($\sim 1''$) across all wavelengths.

[Emsellem et al. \(2022\)](#) processed the PHANGS-MUSE spectral cubes and provide, among several data products, the maps of emission in the H α and H β lines. We took those maps and convolved and re-gridded them to match the resolution of the rest of our data (18"). Pixels with NaN values were treated with interpolation during the convolution. However, if those pixels are at the edge of the map there are not enough nearby values and the interpolation might be unsuccessful. Such pixels are not considered in our analysis. We finally estimated the BD from the ratio of the convolved and re-gridded emission line maps. The approach of estimating the BD after smoothing the maps at the desired spatial resolution is physically accurate and in addition helps to recover the signal in some pixels of the H β maps.

Since this line is less bright than H α , by smoothing the maps we enhanced its S/N and obtained better coverage of the BD map.

The BD is usually converted into a V-band attenuation using

$$A_{\text{V,BD}} = \frac{2.5 \left[\log_{10}(F_{\text{H}\alpha}/F_{\text{H}\beta}) - \log_{10}(F_{\text{H}\alpha}/F_{\text{H}\beta})_0 \right]}{k(\text{H}\beta) - k(\text{H}\alpha)}, \quad (3)$$

where the term at the numerator is the difference between the attenuations in the two Balmer lines, $A_{\text{H}\beta,\text{BD}} - A_{\text{H}\alpha,\text{BD}}$, as derived from the observed BD and its intrinsic (i.e. unattenuated) value, $(F_{\text{H}\alpha}/F_{\text{H}\beta})_0$; that at the denominator is the difference between the attenuation laws (normalised to the V band). We used $(F_{\text{H}\alpha}/F_{\text{H}\beta})_0 = 2.86$ as given by the assumption of a Case B recombination with a typical electron density of 10^{-4}cm^{-2} and a temperature of 10 000 K, as for HII regions ([Hummer & Storey 1987](#); [Osterbrock & Ferland 2006](#)), similarly to what has been done in previous studies (e.g. [Kreckel et al. 2013](#); [Momcheva et al. 2013](#); [Piotrowska et al. 2020](#)). We also used $k(\text{H}\alpha) = 0.77$ and $k(\text{H}\beta) = 1.18$ from [Kreckel et al. \(2013\)](#), which are very close to the values for the average ($R_V = 3.1$) MW extinction law of [Fitzpatrick \(1999\)](#).

2.3. Spectral energy distribution modelling

We used the CIGALE SED-fitting code (see [Boquien et al. 2019](#), and references therein) to model the SEDs of each pixel of the galaxies in our sample and retrieve maps of physical properties, such as the stellar mass (M_{star}), dust mass (M_{dust}), star formation rate (SFR), and A_V . Having defined a grid of values for the parameters of the various modules for the stellar, gas, and dust components and taking into account the dust attenuation, CIGALE creates a library of model SEDs which compares to the multi-wavelength observations in order to select the model SED that best fits the data, through Bayesian inference. CIGALE includes all the different components in such a way that the amount of energy absorbed and re-emitted by the dust grains is fully conserved ([Noll et al. 2009](#); [Roehlly et al. 2014](#)).

Since we aim to investigate properties of a subset of galaxies that belong to the DustPedia sample, our parameter space is based on the parameter grid used in the reference DustPedia sample introduced by [Nersesian et al. \(2019\)](#), see their Table 1), which has also been applied successfully to other samples of local galaxies (see e.g. [Paspaliaris et al. 2021, 2023](#)). A flexible SFH is used, allowing for a late instantaneous burst or quenching episode 200 Myr before the current moment (i.e. module 'sfhdelayedbq'; [Ciesla et al. 2015](#)). The stellar population is thus separated in two components, an old one with age >200 Myr and a young population with age <200 Myr. We assume an initial mass function, as given by [Salpeter \(1955\)](#), of between 0.1 and 100 M_{\odot} , and use the [Bruzual & Charlot \(2003\)](#) stellar population model. In addition to the typical stellar metallicity value of $Z = 0.02$ often used, (e.g. [Boquien et al. 2019](#); [Nersesian et al. 2019](#); [Paspaliaris et al. 2021, 2023](#)), we also considered $Z = 0.008$, and allowed the fitting algorithm to determine the optimal stellar metallicity values between the two options. To model the gas metallicity, we used the radial metallicity gradients from O/H abundances, as derived by [Brazzini et al. \(2024\)](#) with the reliable direct method based on electron temperature measurements. These gradients for our sample are rather flat with central metallicities reaching the solar value. For each galaxy we have the sampled radial variations in the gas metallicity across the star-forming disc and, depending on its gradient, we have established from one (flat gradient) up to three possible values of gas metallicities. These are

all within the two metallicity values considered for the stellar population. The emission from the stellar components as well as from the ionised gas surrounding massive stars (i.e. nebular emission) are attenuated using the same power-law-modified starburst attenuation curve (i.e. module 'dustatt_calzleit'; Calzetti et al. 2000, for $150 \text{ nm} < \lambda < 2200 \text{ nm}$; Leitherer et al. 2002, for $91.2 \text{ nm} < \lambda < 150 \text{ nm}$). The power-law slope is a free parameter modifying the attenuation curve for each fit. Following previous studies (e.g. Noll et al. 2009; Boquien et al. 2012, 2016; Nersesian et al. 2019) the amplitude of the UV bump is set to be zero. The UV emission in our sample is covered by just the two GALEX bands. To better constrain the bump, additional data and preferably NUV spectra (Buat et al. 2012) are required, currently not available for our sample. However, we investigated how a non-zero UV bump amplitude might affect our results by running also CIGALE after setting the UV bump amplitude to the highest value suggested by Battisti et al. (2025) (that uses *Swift*/UVOT NUV data). We did not find sensible variations in the CIGALE results. The attenuation of each stellar population can be estimated separately and depends on two additional free parameters, the colour excess of the young stars and the attenuation-reduction factor for the old stars. The attenuation of the young stars is derived by their estimated colour excess, which is allowed to take 15 possible values varying between zero and one. The attenuation of the light from the old stellar population can be inferred through the reduction factor, which is multiplied to the attenuation of the young stars and is allowed to take three possible values (i.e. 0.25, 0.50, 0.75). The THEMIS model (Jones et al. 2017) is used to account for dust emission.

Separate runs were performed for each galaxy in our sample. The number of free parameters used in the current analysis is 11 and the parameter space does not change from pixel to pixel within a galaxy. As was discussed above, the only parameter whose range might vary from galaxy to galaxy is the gas metallicity. The total number of models produced for each galaxy varies depending on the number of possible values we set for each free parameter, ranging from 99 792 000 to 299 376 000. We would like to stress that in order to keep the maximum number of models at a tolerable level for our available computational power, in favour of setting metallicity as a free parameter, we reduced the possible values of some parameters, such as (i) the galaxy's e-folding time (τ_{main} [Myr]) by removing two, 1700 and 3900, out of ten values, (ii) the fraction of small hydrocarbon solids (q_{hac}) by removing one (0.28) out of 11 values, and (iii) the minimum interstellar radiation field (U_{min} [Habing]), for which we use 12 instead of 14 values, by removing 0.15 and by substituting 0.5, 0.8 by 0.6 and 1.2 by 1.0. The rest of the parameter grid is shown in detail in Table 1 of Nersesian et al. (2019).

To exclude unreliable estimates of the properties, we used a criterion that is based on the comparison of the best-model value (best) and the likelihood-weighted mean value (bayes) estimated by CIGALE, for each pixel. This has been also adopted in other recent studies (e.g. Buat et al. 2021; Mountrichas et al. 2022; Koutoulidis et al. 2022; Chakraborty et al. 2025). Specifically, we consider in our analysis only pixels where $\frac{1}{5} \leq \frac{\text{best}}{\text{bayes}} \leq 5$, for the SED-fitting-derived properties. The bayes value weights all models allowed by the parameter grid, with the best-fit model having the heaviest weight (Boquien et al. 2019). The weight is based on the likelihood, $e^{-\chi^2/2}$, associated with each model. A large difference between the two values (i.e. best, bayes) indicates that the fitting did not achieve a reliable estimation of the corresponding parameter. From this crite-

rium, only 24 pixels (1%) were rejected from NGC 0628, 58 pixels (2.7%) from NGC 3351, 13 pixels (1.5%) from NGC 3627, 3 pixels (0.6%) from NGC 4254 and 57 pixels (3.5%) were rejected from NGC 4321.

As is described in Sect. 2.1.1, we discarded the SPIRE 350 μm and 500 μm bands in order to conduct the analysis at higher spatial resolution. However, the choice has minimal consequence on the estimation of the dust luminosity and mass, as we found by performing three independent SED-fitting analyses for one of our targets, NGC 0628. Each time, we used different spectral coverage (i.e. up to 500 μm , up to 350 μm , and up to 250 μm) and resolution (i.e. 36'', 25'', and 18'', respectively) and created the radial profiles of Σ_{dust} using bin-widths equal to the resolution of each case. For all cases, we retrieved the same radial profile with the data lying within the uncertainties. We observed a mild overestimation of Σ_{dust} when we omitted the 500 μm band, or both 500 μm and 350 μm bands, at a maximum of less than a factor of two, towards the very central part of the galaxy. In a recent study, Chastenot et al. (2024) also shows that the trends and parameter values are well reproduced without considering the two longer wavelength SPIRE bands.

A suite of maps of several parameters for NGC 4321 are shown in Fig. 1, as an example. In the top left panel, we show the convolved and re-gridded SDSS r band for a visual inspection of the morphological structure of the galaxy. The rest panels in the top row show maps of SED-fitting-derived properties ($\log_{10} \Sigma_{\text{star}}$, $\log_{10} \Sigma_{\text{SFR}}$, $\log_{10} \Sigma_{\text{dust}}$, $A_{V,\text{SED}}$, from left to right). The bottom panels consist of maps of Σ_{HI} , Σ_{H_2} , $\log_{10} \Sigma_{\text{gas}}$, $\Sigma_{\text{dust}}/\Sigma_{\text{gas}}$ and $A_{V,\text{BD}}$, from left to right. The corresponding maps of all galaxies in our sample can be found in Appendix A.

2.4. Data analysis: Geometries and statistical methods

When comparing dust and gas surface densities, we considered face-on values, applying inclination corrections to each galaxy, under the assumption that the ISM is distributed in a thin disc. Attenuations may or may not be inclination-dependent according to the geometrical distribution of the medium providing the attenuation in the case of the $A_{V,\text{BD}}$, or to how dust is distributed with respect to the stellar component if we refer to the attenuated stellar light. For the attenuation inferred by the BD, in the molecular phase for example, inclination corrections are less meaningful because molecular clouds have nearly spherical geometry. Consequently, in plotting the attenuation versus dust surface densities we refer to line of sight values (denoted by the LOS suffix) whether we consider dust mixed with the stars or distributed in a shell around star-forming regions (as also done by Boquien et al. 2013; Kreckel et al. 2013). For completeness, we briefly discuss the correlation coefficients for face-on values as well.

To estimate the scaling relations, we performed fitting through Bayesian inference using the Python UltraNest package (Buchner 2021). UltraNest derives posterior probability distributions and the Bayesian evidence with the nested sampling Monte Carlo algorithm MLFriends (Buchner 2016, 2019). This method provides a robust estimate of the scaling relations between two quantities incorporating the uncertainties of both quantities directly into the fitting process, leading to more reliable estimations of the fitted parameters (i.e. slope and intercept) and their uncertainties. For each correlation we also provide the corresponding statistical coefficients that indicate its significance, i.e. Pearson's (ρ_P) and Spearman's (ρ_S) coefficients.

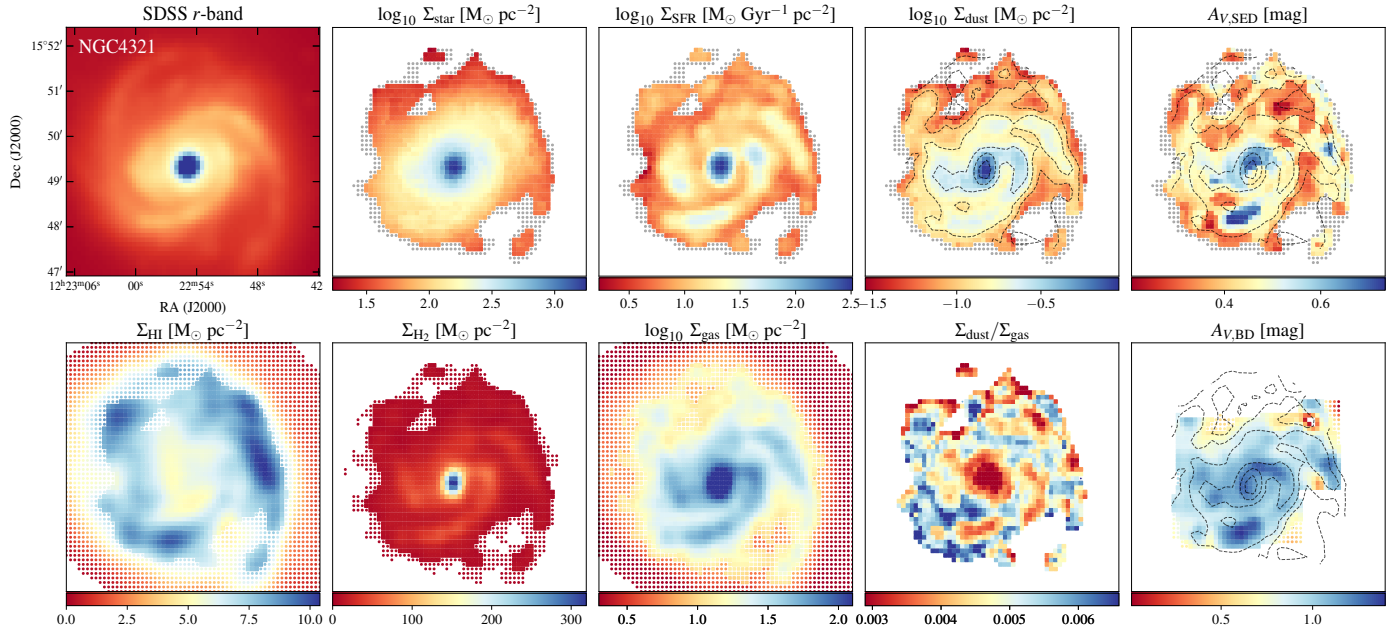


Fig. 1. Maps of observed and derived properties of NGC 4321. Top: Convolved and re-gridded SDSS r band, logarithms of stellar mass surface density (Σ_{star}), SFR surface density (Σ_{SFR}), dust mass surface density (Σ_{dust}), as well as SED-fitting-derived attenuation in the V band ($A_{V,\text{SED}}$), from left to right. Bottom: Surface density of atomic gas mass (Σ_{HI}), surface density of molecular gas mass (Σ_{H_2}), logarithm of the total gas mass surface density (Σ_{gas}), dust-to-gas ratio and attenuation in the V band as derived by the BD ($A_{V,\text{BD}}$), from left to right. All maps are at a resolution of $18''$. Grey points correspond to pixels that are rejected because they do not have a sufficient number of data points in the FIR regime (see Sect. 2.1.1) or because they are unreliable (see Sect. 2.3 for more details). The Σ_{HI} and Σ_{H_2} maps extend up to their corresponding 3σ limit. In the Σ_{HI} , Σ_{H_2} , and $A_{V,\text{BD}}$ maps pixels that correspond to the areas that are excluded by the SED-fitting analysis are plotted with smaller dots. In the $\log_{10} \Sigma_{\text{gas}}$ map, pixels excluded by the SED-fitting analysis and having both HI and CO detection are depicted by smaller squares, while pixels with only HI and not CO are plotted with dots. In the dust-to-gas ratio maps, we limit the colour-coding to the 5th–95th percentile range for illustrative purposes. Contours are taken from the $\log_{10} \Sigma_{\text{dust}}$ [$M_{\odot} \text{pc}^{-2}$] maps with a lowest contour at -1.5 and linear spacing with the highest at 0.

3. Results and discussion

The availability of a wide range of multiwavelength data for our galaxies allows us to examine the relation of dust in emission (Σ_{dust}) with atomic gas traced by HI (Σ_{HI}), molecular gas traced by CO(2-1) (Σ_{H_2}) and the total gas (Σ_{gas}), as well as the correlation of optical attenuation derived from the BD ($A_{V,\text{BD}}$) and the stellar light attenuation inferred by SED fitting ($A_{V,\text{SED}}$), with Σ_{gas} and Σ_{dust} . Based on the A_V – Σ_{dust} relation, we investigate the dust spatial distribution using also predictions from simple radiative transfer models. Moreover, we compare $A_{V,\text{BD}}$ to $A_{V,\text{SED}}$. The correlations among these physical properties are explored in a resolved scale (346 pc, on average; see the pixel size of each galaxy in Table 1).

The necessity of using only high-S/N pixels for the derivation of the physical properties through the SED-fitting analysis, limits our study to the main part of the star-forming disc. Moreover, in the discussed correlations that include the $A_{V,\text{BD}}$, we are slightly more limited to the inner part of the disc observed by MUSE. Thus, all the following correlations discussed here do not refer to the outskirts of the galaxies where the ISM is mostly atomic.

3.1. Dust mass surface densities as gas tracers

We examine here which gas phase establishes the best correlation with dust. In Fig. 2 we present the relations between the dust and the gas mass surface densities for galaxies in our sample. More specifically, in the left panel we show the $\log_{10} \Sigma_{\text{dust}}$ – $\log_{10} \Sigma_{\text{HI}}$ relation, in the middle panel the relation between $\log_{10} \Sigma_{\text{dust}}$ and $\log_{10} \Sigma_{\text{H}_2}$, while the correlation of the $\log_{10} \Sigma_{\text{dust}}$ with the total gas, $\log_{10} \Sigma_{\text{gas}}$, is displayed in the right panel.

Although on average galaxies with higher Σ_{dust} have also higher Σ_{HI} , the left panel of Fig. 2 shows that these two quantities have a moderate correlation ($\rho_P = 0.55$; $\rho_S = 0.53$ in the log-log plane) because inside each galaxy Σ_{dust} is not often dependent on Σ_{HI} . The average fitted slope is 0.63 ± 0.01 and a significant scatter of 0.25 ± 0.002 is present. An exception is NGC 3627 for which a moderate correlation is found on a resolved scale of 330 pc ($\rho_P = 0.67$; $\rho_S = 0.66$; slope: 0.94 ± 0.04 , scatter: 0.11).

The middle panel of Fig. 2 shows instead that $\log_{10} \Sigma_{\text{dust}}$ strongly correlates with $\log_{10} \Sigma_{\text{H}_2}$ having $\rho_P = 0.91$ and $\rho_S = 0.90$. The slope of the linear correlation is 0.67 ± 0.004 with a scatter of only 0.09 ± 0.001 . The correlation holds also for individual galaxies for which slopes are similar to the global one. An increase in the scatter in the low Σ_{H_2} regime, is a consequence of higher Σ_{dust} variations in galaxy’s outskirts and in addition here the use of a constant α_{CO} might not be totally appropriate (see discussion in Appendix B). The sublinear slope between $\log_{10} \Sigma_{\text{dust}}$ and $\log_{10} \Sigma_{\text{H}_2}$ simply states that dust distributions have shallower radial gradients than molecular gas distributions. Assuming that gas and dust can be described by radially exponential discs, it is straightforward to show that the correlation between Σ_{dust} and Σ_{H_2} is the inverse of their scale-length ratios. From the slope of the linear fit in the $\log_{10} \Sigma_{\text{dust}}$ – $\log_{10} \Sigma_{\text{H}_2}$ relation, the dust scale-length is thus ~ 1.5 times larger (on average) than the molecular gas scale-length. This is compatible with other results in the literature: for instance, Casasola et al. (2017) fit radial exponential profiles to Σ_{H_2} and Σ_{dust} and find that, for their sample, the radial scale-length of the dust disc is on average about twice that of the molecular gas disc. We remind here that we have assumed constant values for the CO-to- H_2

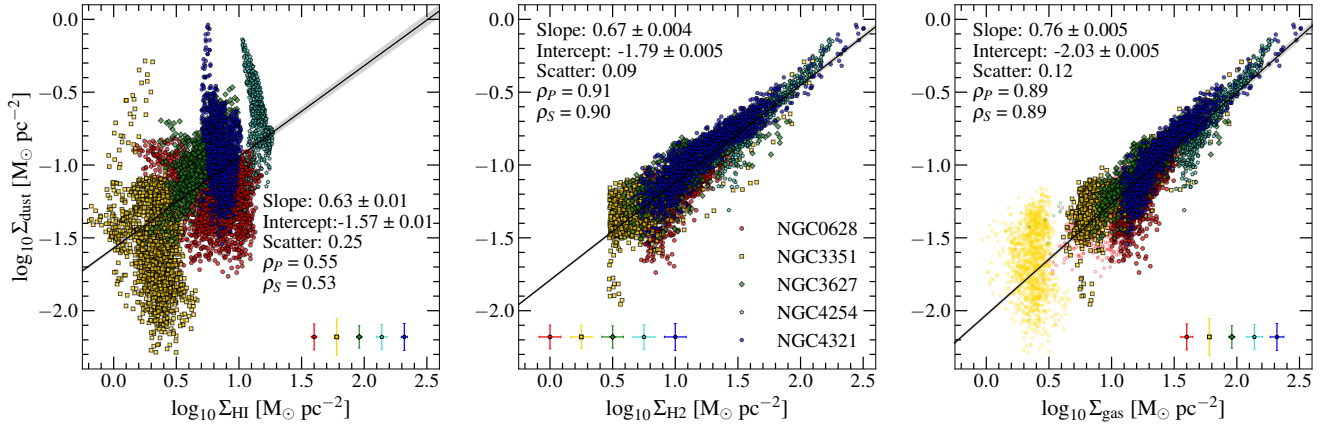


Fig. 2. Resolved scaling relations of dust mass surface density with the atomic (left panel), molecular (middle panel) and total gas (right panel) surface density. Each galaxy is represented by a different colour. The median uncertainties for each galaxy are shown in the lower right or lower left corner of the panels. The solid lines are the best linear fits to the full sample, while the shaded grey area indicates the fit uncertainty. The slope, intercept, and scatter of each fit are also given along with the correlation coefficients. In the right panel open circles show pixels where only HI is detected.

conversion factors. If instead there are radial variations in α_{CO} (and/or R_{21}), the gradient of the molecular gas might be different from that inferred from the CO distribution. Several studies have found that α_{CO} increases radially (see e.g. Bolatto et al. 2013; Chiang et al. 2024, and Appendix B). A radially increasing α_{CO} would give a flatter radial profile of Σ_{H_2} , closer to the Σ_{dust} gradient (in this case the slope of the Σ_{dust} and Σ_{H_2} correlation increases). For instance, using one of the radial dependent α_{CO} recipes suggested by Chiang et al. (2024), we found that the average slope of the correlation increases, from 0.67 to 0.77 (i.e. the dust scalelength is $1.3\times$ that of molecular gas); however, there is no significant improvement in the correlation strength or in the scatter (see Fig. B.2).

A similar correlation, but with a steeper slope (0.76 ± 0.005), is found between $\log_{10} \Sigma_{\text{dust}}$ and $\log_{10} \Sigma_{\text{gas}}$, as shown in the right panel of Fig. 2. Here $\rho_P = 0.89$, $\rho_S = 0.89$, and a scatter of 0.12 ± 0.001 are found, larger than for the $\log_{10} \Sigma_{\text{dust}} - \log_{10} \Sigma_{\text{H}_2}$ relation. The correlation parameters remain unchanged if we omit pixels where only atomic gas is detected (open circles). The strength of the correlation between $\log_{10} \Sigma_{\text{dust}}$ and $\log_{10} \Sigma_{\text{gas}}$ (Fig. 2, right panel), is almost the same as that with the molecular gas only. This reflects the fact that the gas in the regions examined has a large contribution by the molecular phase. The steeper slope of the correlation is due to the increased contribution of atomic gas at large galactocentric distances. As for the relationship with the molecular gas only, the $\log_{10} \Sigma_{\text{dust}} - \log_{10} \Sigma_{\text{gas}}$ correlation seems to depend marginally on the properties of the sampled galaxies. This is in agreement with the findings of Abdurro'uf et al. (2022) that find no significant galaxy-by-galaxy variations in $\Sigma_{\text{dust}} - \Sigma_{\text{H}_2}$ and $\Sigma_{\text{dust}} - \Sigma_{\text{gas}}$ relations. By estimating the best-fit parameters for each galaxy individually, we notice that only the Virgo galaxies (NGC 4254, NGC 4321) have a steeper correlation (slope: 1.04 ± 0.01 , 0.84 ± 0.01 , respectively) than the mean slope. These findings hold also when we adopt a radially dependent α_{CO} .

3.2. Molecular gas shielding layers and the dust-to-gas ratio

In the left panel of Fig. 2 we notice that every galaxy has a narrow range of Σ_{HI} ; these vary only by a factor 2–3 across the disc extent we are examining, with the mean value for each galaxy that changes by about 0.8 dex across the sample. What drives the changes of the mean HI column den-

sity from one galaxy to another? One possibility is that variations in the mean Σ_{HI} from galaxy to galaxy are related to molecular shielding. Variations in the shielding HI surface densities might be connected to variations in the dissociating radiation field, of volume gas densities or of the dust-to-gas mass ratio ($\text{DGR} = \Sigma_{\text{dust}}/\Sigma_{\text{gas}}$). For the DGR we expect Σ_{HI} to increase as the DGR decreases. The average DGRs found in the sampled regions are 0.0033 ± 0.0005 , 0.0041 ± 0.001 , 0.0048 ± 0.0010 , 0.0054 ± 0.0013 and 0.0069 ± 0.0020 , for NGC 4254, NGC 0628, NGC 4321, NGC 3627 and NGC 3351, respectively. NGC 4254 is the richest galaxy in gas content and it shows the lowest DGR. Because of this low DGR, the galaxy needs the largest Σ_{HI} of the sample to shield the molecular phase. On the contrary, NGC 3351 has a low gas content and the highest DGR of our sample. Molecules in this case are shielded using a much lower HI column density than for NGC 4254.

The increase in the mean Σ_{dust} within the Σ_{HI} range for each galaxy might indicate an increase in Σ_{gas} , i.e. an increase in the molecular fraction. To verify this in Fig. 3 we plot the $\log_{10} \Sigma_{\text{dust}}$ as a function of $\log_{10} \Sigma_{\text{HI}}$, colour coded with atomic gas fraction ($f_{\text{HI}} = M_{\text{HI}}/M_{\text{gas}}$) in the top panel and with $\log_{10} \Sigma_{\text{star}}$ in the bottom panel. For each galaxy f_{HI} decreases going towards regions with higher dust, indicating an increase in the total gas column density, with the gas becoming more molecular. The bottom panel of Fig. 3 underlines in fact that regions with higher Σ_{dust} are places where also Σ_{star} is higher, i.e. the gas layer has higher densities being more compressed by the local stellar gravity, and the formation of molecules is enhanced.

We finally examine in Fig. 4 how the molecular gas fraction ($f_{\text{H}_2} = M_{\text{H}_2}/M_{\text{gas}}$) varies as a function of the DGR for each galaxy. We find that Sc galaxies (NGC 0628, NGC 4254) have a marginal positive trend with higher f_{H_2} where the DGR is higher, while Sb galaxies hosting a bar (NGC 3351, NGC 3627) have a negative trend on average. A peculiar case is NGC 4321 (SABb) where a transition is observed with pixels having $f_{\text{H}_2} \lesssim 0.8$ (outer disc) exhibiting no correlation (or a positive correlation for $f_{\text{H}_2} \lesssim 0.6$), while pixels with higher f_{H_2} (central area) having a negative correlation with the DGR. By visually inspecting the DGR map in Fig. 1 we notice the low values in the central area and the rather inhomogeneous distribution in the rest of the disc. The scatter is generally large as in NGC 3351. Here, mainly the central pixels show some correlation with the DGR.

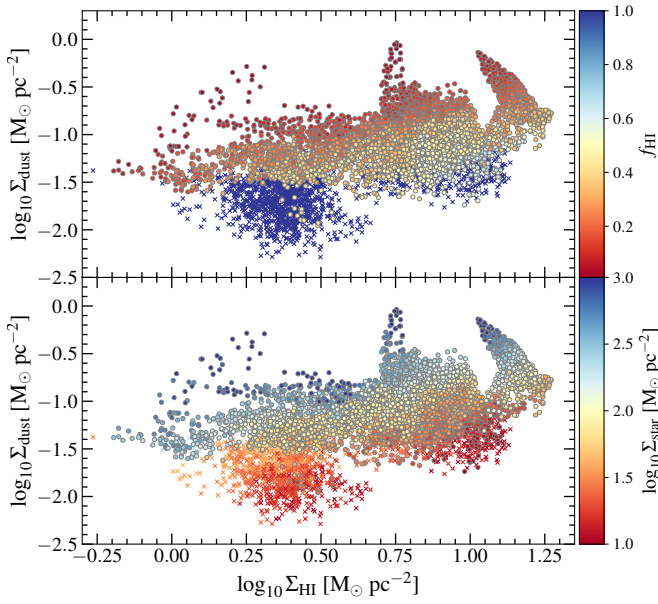


Fig. 3. Dust mass surface density as a function of atomic gas mass surface density, colour-coded with atomic gas mass fraction (top panel) and stellar mass surface density (bottom panel) for the whole sample. In both panels, crosses refer to pixels where only HI gas is detected.

Our findings might indicate a morphological evolution between Sc and Sb galaxies, possibly related to the presence of a bar. The bar might drag material (dust and gas) towards the centre of the galaxies; during this process, a significant part of the dust can be destroyed by the intense stellar radiation field in that area. This might explain why the DGR remains constant or decreases, while the molecular gas fraction can still increase towards the centre. This is apparent also in the DGR maps (see the corresponding maps in Fig. 1 and Appendix A), where all barred galaxies exhibit a dust-poor centre. Another possibility is that central regions have a lower α_{CO} or a higher R_{21} , as we discuss in detail in Appendix B. For the rest of the discs, given the relatively flat metallicity gradients estimated by Brazzini et al. (2024), with central metallicities of the order of solar, we do not expect strong variations in α_{CO} . Although α_{CO} and R_{21} variations might give a somewhat different relation between f_{H_2} and the DGR, our analysis in Appendix B confirm the trends shown in Fig. 4.

3.3. The relations between $A_{V,\text{BD}}$ and gas mass surface densities

Here we examine the relation between the V-band attenuation as derived by the BD, $A_{V,\text{BD}}$, with cold gas in the ISM. Our results are shown in Fig. 5, where $\log_{10} A_{V,\text{BD}}$ is plotted against $\log_{10} \Sigma_{\text{HI}}$ (left panel), $\log_{10} \Sigma_{\text{H}_2}$ (middle panel) and $\log_{10} \Sigma_{\text{gas}}$ (right panel). The relations have similar scatter and flatter slopes (indicated in each panel) than those found between Σ_{dust} and Σ_{gas} . Similarly to what we find for the $\log_{10} \Sigma_{\text{dust}} - \log_{10} \Sigma_{\text{HI}}$ relation, in the left panel of Fig. 5 we see that galaxies which have higher Σ_{HI} have also on average higher $A_{V,\text{BD}}$, but locally, in each galaxy, there is no correlation. The global correlation is moderate ($\rho_P = 0.60$; $\rho_S = 0.69$).

For $\log_{10} A_{V,\text{BD}} - \log_{10} \Sigma_{\text{H}_2}$ relation, the positive correlation is clear both for individual galaxies and globally for the whole sample. The correlation is moderate if we rely on the correlation coefficients $\rho_P = 0.62$, but the value of the Spearman coefficient $\rho_S = 0.78$ indicates a stronger correlation of $A_{V,\text{BD}}$ with the molecular gas surface density than with the atomic gas. The

$\log_{10} A_{V,\text{BD}}$ has a similar correlation with the $\log_{10} \Sigma_{\text{gas}}$ than with the $\log_{10} \Sigma_{\text{H}_2}$ ($\rho_P = 0.66$; $\rho_S = 0.82$).

If we correct to face-on values both $A_{V,\text{BD}}$ and gas surface densities, the above correlations weaken, the slopes are flatter and the scatter increases. As mentioned in Section 2.4, corrections to face-on values are linked to the geometrical distribution of physical quantities which are not known a priori for the dust providing the attenuation. The stronger correlations we find for line-of-sight values compared to face-on values suggest that the geometric distribution of the absorbing medium is close to spherical. In this case also the attenuation linked to the atomic gas might be driven by HI envelopes around the star formation regimes rather than by the whole atomic gas disc layer. The correlations found between face-on cold gas mass surface densities and $A_{V,\text{BD}}$ are also weaker than between the same gas surface densities and Σ_{dust} , and underline that only part of the gas and dust mix, present in a galaxy, is responsible for the attenuation of stellar light.

We note that the fitting properties in the $\log_{10} A_{V,\text{BD}} - \log_{10} \Sigma_{\text{gas}}$ relations do not change if we exclude pixels detected only in HI (open symbols). To ensure a robust estimation of the correlation, Barrera-Ballesteros et al. (2020) omit cases exhibiting $A_V[\text{mag}] < 0.2$ thus excluding regions where CO emission likely drops rapidly due to the photo-dissociation of the CO molecules (van Dishoeck & Black 1988). The exclusion of such pixels does not affect our findings concerning the estimated fitting parameters. In addition, motivated by the fact that we trace slightly different physical scales for galaxies in our sample, we examined the variation in the scatter with respect to the pixel width, but we find no trend. We underline that when we use a radially dependent α_{CO} conversion as suggested by the Chiang et al. (2024) recipe, there is a marginal increase in the strength of the corresponding correlations, but the scatter remains similar (see Fig. B.2).

For NGC 3627 we find the highest $A_{V,\text{BD}}$ values among all the regions studied in our sample (confirmed also by the $A_{V,\text{SED}}$). Having this galaxy the highest inclination of all galaxies examined in this paper ($i = 67.5^\circ$) this finding is consistent with what Concas & Popesso (2019) have also found, namely higher BDs in more inclined galaxies. However, some caution is needed for NGC 3627 because the high A_V values are found mainly in the western arm, where an extended polarised radio ridge is, likely caused by ram-pressure compression (Weżgowiec et al. 2012). Ram pressure compression is able to increase locally gas and dust column densities, with a consequent increase in A_V (see e.g. Abramson et al. 2011). Nonetheless, excluding NGC 3627 we find similar correlation coefficients for the line-of-sight $\log_{10} A_{V,\text{BD}} - \log_{10} \Sigma_{\text{H}_2}$ relation ($\rho_P = 0.62$; $\rho_S = 0.76$) and again stronger correlation between $\log_{10} A_{V,\text{BD}}$ and $\log_{10} \Sigma_{\text{gas}}$ ($\rho_P = 0.66$; $\rho_S = 0.82$), as well as slopes and scatters similar to the ones found for the full sample.

3.4. Comparison of $A_{V,\text{BD}}$ and $A_{V,\text{SED}}$

A visual inspection of the A_V maps displayed in Fig. 1 and Appendix A shows that the attenuations computed via BD and SED fitting have a similar pattern across the discs, although $A_{V,\text{BD}}$ is systematically higher than the $A_{V,\text{SED}}$. This is also shown in the left panel of Fig. 6, where the A_V derived from the two independent methods are compared. If we focus on the star-forming regions with $\Sigma_{\text{SFR}} [\text{M}_\odot \text{Gyr}^{-1} \text{pc}^{-2}] > 100$ (white data points) the dispersion is reduced. By performing a linear best-fitting analysis on the star-forming regions we find that

$$A_{V,\text{SED}} = (0.59 \pm 0.05) A_{V,\text{BD}}.$$

The slope of our best-fitted linear relation, shown with a dashed line, is slightly higher than the value found for the relation

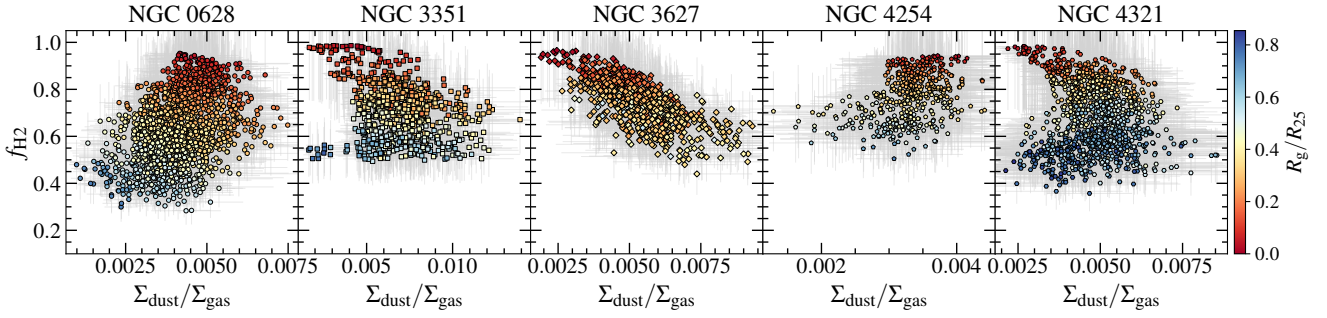


Fig. 4. Molecular gas mass fraction as a function dust-to-gas mass ratio, for each galaxy in the sample. The data points are colour coded as a function of galactocentric radius in units of R_{25} . Uncertainties are plotted by grey error bars.

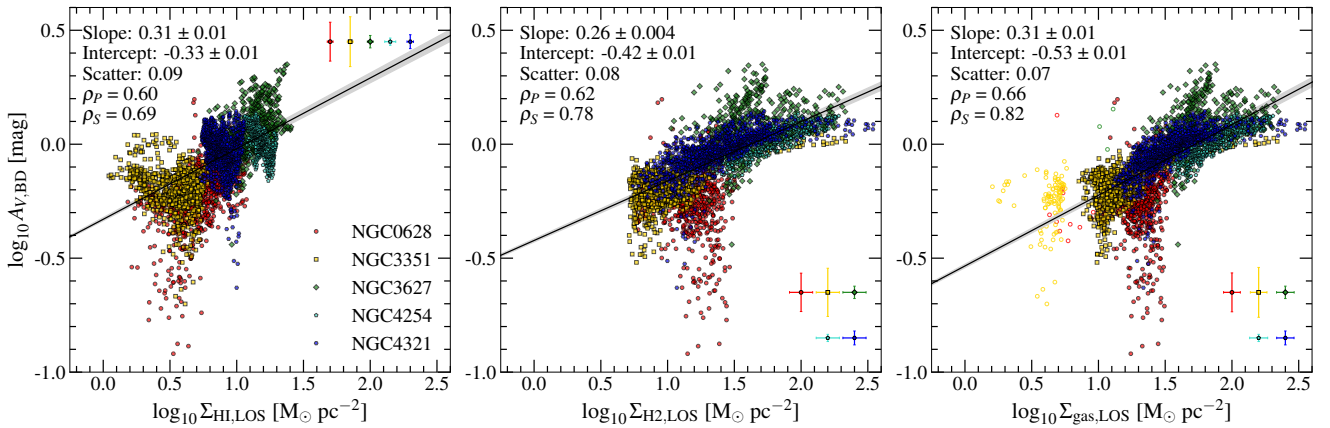


Fig. 5. Attenuation on the V band, derived from the BD, as a function of the line-of-sight surface density of the atomic (left panel), molecular (middle panel) and total gas (right panel) mass. Each galaxy is represented by a different colour. The median uncertainties for each galaxy are shown in the top or the lower right corner of the panels. The solid lines are the best linear fits to the full sample, while a shaded area indicates the fit uncertainty. The slope, intercept, and scatter of each fit are also given along with the correlation coefficients.

between emission line and stellar continuum A_V by Calzetti et al. (2000) (dash-dotted line, slope 0.44) and Kreckel et al. (2013) (dotted line, slope 0.47). We underline that this result is sensitive to the selected attenuation law (i.e. the $k(H\alpha)$, and $k(H\beta)$ values used in Eq. (3)). In principle, the attenuation law found for each pixel by our SED-fitting analysis, under the assumption of a modified power-law starburst attenuation curve (see Sect. 2.3), might result in a different conversion factor between $F_{H\alpha}/F_{H\beta}$ and $A_{V,BD}$. Nevertheless, we found that, when averaging over all pixels, the factor is very close to that adopted by Kreckel et al. (2013) and thus we use a uniform conversion factor.

The selected SFH and attenuation modules used in our SED-fitting analysis allow us to estimate separately the attenuation on the emission of the old and the young stars. In Fig. 6 middle and right panels, we compare $A_{V,BD}$ with the attenuation on the old ($A_{V,SED}^{old}$) and young stars ($A_{V,SED}^{young}$), respectively. We find that the total attenuation estimated by CIGALE is dominated by $A_{V,SED}^{old}$, which is expected, since the bulk of the total stellar content in spiral galaxies is dominated by old stars (see e.g. Nersesian et al. 2019; Paspaliaris et al. 2023). The $A_{V,SED}^{young}$ though, despite the larger uncertainties, is in a quite good agreement with the $A_{V,BD}$, with the bulk of the data points following the one-to-one relation and 88.6% of them lying within 0.5 dex (dashed grey lines). This indicates that CIGALE is able to estimate the attenuation in star-forming regions on resolved scales, using broadband photometric data only (see also the comparison of the BD-inferred attenuation and SED-fitting-derived attenuation of the birth clouds, in global scales, by Kouroumpatzakis et al. 2021). In a future

study, it would be interesting to investigate if the scatter and the uncertainties might decrease by enriching the relative free parameters in the SED fitting with more values and/or by including also narrowband photometric data (e.g. $H\alpha$ maps) that are available for all the galaxies in our sample. A plateau found at $A_{V,BD} \sim 1.3$ mag, might be attributed to the fact that $A_{V,BD}$ and $A_{V,SED}^{young}$ trace different environments with different optical depths at high attenuation values (see also Sect. 3.5 where, at high attenuations, $A_{V,SED}^{young}$ is more closely connected with a dust screen configuration than the $A_{V,BD}$).

3.5. The correlation of dust in absorption and dust in emission

A visual comparison of the spatial distribution of Σ_{dust} , $A_{V,BD}$ and $A_{V,SED}$ across galaxies' discs can be done using the maps of Fig. 1 and Appendix A, where contours of Σ_{dust} are overlaid in all three maps. The pixel-by-pixel relation for each galaxy is shown in Fig. 7 using the $A_{V,BD}$ (left panel), the $A_{V,SED}^{old}$ (middle panel) and the $A_{V,SED}^{young}$ (right panel). The number of data points is smaller in the first panel because of the restricted extent of MUSE data, compared to the CIGALE SED-fitted area. We observe an increasing trend of Σ_{dust} with $A_{V,BD}$ and $A_{V,SED}^{young}$, rather than $A_{V,SED}^{old}$ that increases milder as a function of Σ_{dust} . This suggests that nebular lines and young stars are more sensitive tracers of the dust mass surface density in our sample. Our finding is in agreement with the results of Muñoz-Mateos et al. (2009)

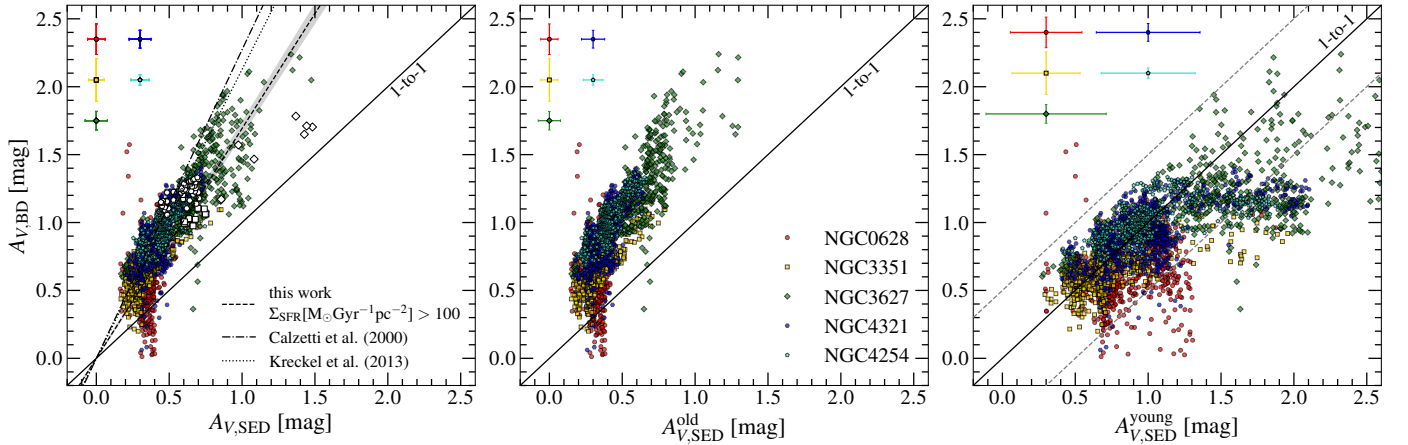


Fig. 6. Correlation between the V -band attenuation derived by BD and SED fitting (total, old, and young stars, in the left, middle, and right panels, respectively). Each galaxy is represented by a different colour. A solid line stands for the one-to-one relation. Left panel: $A_{V,BD}$ versus the total attenuation estimated by CIGALE ($A_{V,SED}$). Points with $\Sigma_{SFR} [M_{\odot} \text{Gyr}^{-1} \text{pc}^{-2}] > 100$ are shown in white. The best-linear fit to the latter points, assuming a zero intercept, is plotted with a dashed line and its uncertainty is indicated by the shaded grey area. A dash-dotted and a dotted line represent the corresponding results from Calzetti et al. (2000) and Kreckel et al. (2013). Middle panel: $A_{V,BD}$ versus the attenuation of the old stellar component as estimated by CIGALE ($A_{V,SED}^{\text{old}}$). Right panel: $A_{V,BD}$ versus the attenuation of the young stellar component as estimated by CIGALE ($A_{V,SED}^{\text{young}}$). The plus-minus 0.5 dex area is defined by the dashed grey lines.

who used the total IR-to-UV ratio, tracing intermediate age stars, to measure the attenuation, and *Spitzer* imaging to estimate the radial dust properties of nearby galaxies. We also find our results in agreement with those of Kreckel et al. (2013) whose method of analysis is more similar to that adopted in the current study.

The quantity A_V is proportional to the dust surface density only when dust is distributed in a ‘screen’ in front of the sources. Σ_{dust} can be directly converted into A_V after assuming a DGR (see Eq. (4) in Kreckel et al. 2013). This foreground screen model is shown in Fig. 7, where we use the DGR of the THEMIS model, equal to 0.0074. For the same surface density, lower extinctions can be obtained if dust and stars are distributed in the same layer (the ‘slab’ model; Disney et al. 1989; Calzetti et al. 1994); and even lower if the dust layer is internal to the stellar one (the ‘sandwich’ model; Disney et al. 1989), as emerges from radiative transfer analyses of edge-on galaxies (Xilouris et al. 1999; Bianchi 2007; De Geyter et al. 2013). Results from the slab and sandwich models are shown in Fig. 7. Rather than the analytical solution for a non-scattering medium (Disney et al. 1989) or approximations to include scattering (Calzetti et al. 1994; Kreckel et al. 2013; Boquien et al. 2013) we made a full radiative transfer calculation using the TRADING code (Bianchi 2008), assuming that the thickness of the dust layer is the same (for the slab) or half (for the sandwich) that of stars, and adopting the average properties of the THEMIS model (see Appendix C for details). $A_{V,BD}$ for the slab and sandwich models, derived using Eq. (3), are shown by the dotted and dash-dotted lines of Fig. 7 (left panel), respectively. It is worth noting that $A_{V,BD}$ is not a direct measure of A_V and in particular the two quantities diverge for high dust column densities (optical depths). We plot A_V for our models in the central and right panel of Fig. 7. The difference is due to the fact that Eq. (3) is formally correct only when the effective attenuations driving the difference between the observed and intrinsic $F_{H\alpha}/F_{H\beta}$ follow the same attenuation law, described by the $k(H\alpha)$ and $k(H\beta)$ values used in the formula. Instead, constant values are used in Eq. (3), while the true attenuation laws change with dust column density because of radiative transfer effects. This is true not only for the models shown in the figure, but also for simpler cases with no scattering (see Appendix C). However, for the surface density

range shared by most pixels, A_V and $A_{V,BD}$ have similar trends and can be considered as lower limits to the V -band attenuation for our pixels. We also derived attenuations for an exponential model with parameters similar to those derived by fits of edge-on galaxies, but found little differences with the sandwich model (not shown here).

The left panel of Fig. 7 shows that $A_{V,BD}$ is close to the screen model for low Σ_{dust} pixels, while it lies between the screen and the slab at higher surface densities. This suggests that the dust that obscures the emitters in the star-forming areas are distributed in a mixed dust and emitting material, as well as a foreground screen dust component. Kreckel et al. (2013) reached similar conclusions, though their best fit to the $A_{V,BD} - \Sigma_{\text{dust}}$ correlation (dashed line) tend to be shifted towards higher surface densities; beside differences in the sample and analysis, this could be in part due to different dust emission templates used to derive Σ_{dust} (they use those of Draine et al. 2007, which results in dust masses larger by about 50% with respect to those derived using THEMIS; see Nersesian et al. 2019). Our findings are also in accordance with a recent study, in global scales, using GAMA data (i.e. BD and Σ_{dust}), by Farley et al. (2025). In that paper it is found that in the case of low dust content, the foreground screen and the mixed geometry (described as ‘distributed’ in their study) both fall in the low BD region, as neither is able to provide enough attenuation to explain the high BD measurements. Furthermore, they report two distinct cases in which, for high dust content, the dust in the screen model is optically thick and prevents emission lines from escaping, leading to a lack of measurements in that regime. In the case of the mixed geometry, lines originating from stars deeply embedded in dust clouds escape less (i.e. are more attenuated) than the ones in the outer regions, allowing for low BD measurements despite the high Σ_{dust} in these regions.

As was also shown in the previous section, $A_{V,SED}^{\text{young}}$ (right panel of Fig. 7) follows a trend similar to that of $A_{V,BD}$. Despite the large uncertainties, the attenuation estimated for young stars is consistent with that estimated from the BD. Instead, $A_{V,SED}^{\text{old}}$ more closely follows the models in which stars and dust are mixed (middle panel; slab and sandwich are very close for low column densities), suggesting that the radiation from the old

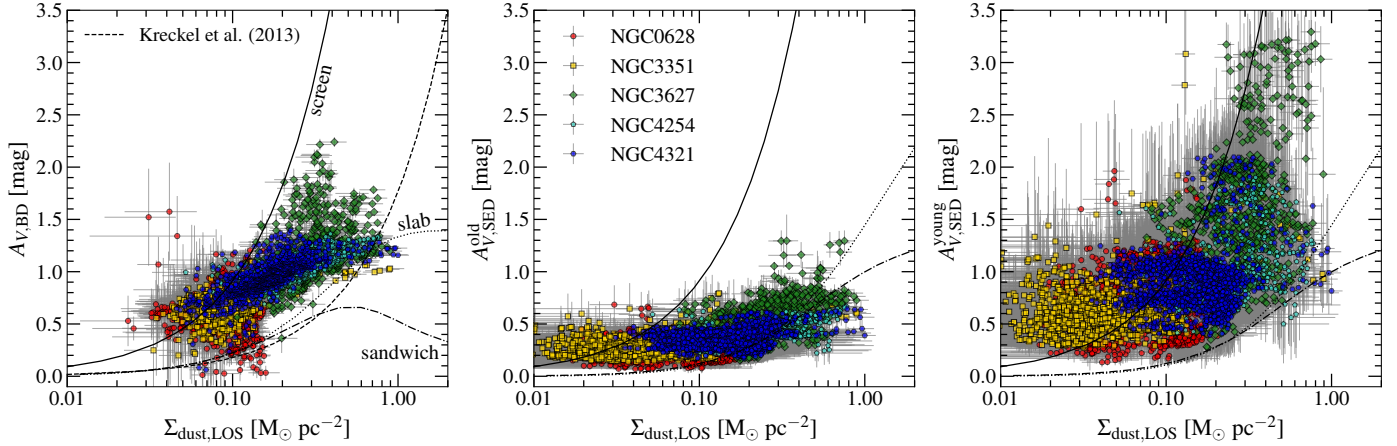


Fig. 7. Relation of line-of-sight dust mass surface density with V -band attenuation derived by the BD (left panel), attenuation of the old stars by the SED fitting (middle panel) and attenuation of the young stars also derived by CIGALE (right panel). Uncertainties in both axes are shown in grey. The dust mass surface density estimated under the assumption of a foreground screen dust model is plotted with a solid line. The dotted and dash-dotted curves show the results of the slab and sandwich models, respectively: those in the left panel are for the $A_{V,BD}$ - Σ_{dust} relation, those in the central and right panel for A_V - Σ_{dust} . The best fit of Kreckel et al. (2013) is plotted with a dashed line in the left panel.

stars is being obscured mainly by the diffuse star-dust geometry of a galactic disc. $A_{V,SED}^{old}$ also shows that the attenuation does not tend to zero at the lowest column densities, but is biased towards a non-null value. Boquien et al. (2013) noted a similar trend, with non-null attenuation at the lowest gas surface densities, and imputed it to the fact that attenuation is a luminosity-weighted quantity while surface densities are mass-weighted means over the finite extent of a resolution element. It is unclear whether this consideration applies also for our case, given the fact that the Σ_{dust} is derived from SED fits to FIR luminosity, unless the biasing due to luminosity weighting acts in different ways on the determination of $A_{V,SED}^{old}$ and Σ_{dust} . Investigating this issue would require a multi-wavelength modelling of a galaxy and the fitting of its SED at different resolutions, which is beyond the scope of the present study.

However, correlations between Σ_{dust} and $A_{V,SED}$ derived by the SED fitting should be interpreted with some caution. The two properties are estimated by the same SED-fitting run and under the assumption of energy balance. Although, despite they are expected to be coupled, they are not tightly constrained by each other alone. For instance, a certain IR luminosity can be produced by different amounts of dust mass, under different heating conditions, which are not tightly constrained by the UV-optical data used to fit the attenuation curve. Alternatively, higher U_{min} (i.e. higher dust temperature) can reduce the need for a high dust mass to explain the IR flux, while still producing a similar attenuation. Indeed, despite the caveat on energy balance our findings regarding the correlations between $A_{V,SED}^{old}$, $A_{V,SED}^{young}$ and Σ_{dust} are in accordance with the picture derived by the RT models.

4. Summary and conclusions

We have investigated the relation between the dust mass surface density (Σ_{dust}), the gas mass surface density (Σ_{HI} , Σ_{H_2} , Σ_{gas}), and the optical attenuation ($A_{V,BD}$, $A_{V,SED}$), throughout the disc of a sample of five nearby spiral galaxies, down to sub-kiloparsec scales. Our main results are summarised as follows:

- In the regions sampled in this study, which have molecular-fraction $f_{H_2} \gtrsim 0.3$, we find that Σ_{dust} and $A_{V,BD}$ are better at tracing the molecular and total gas content rather than the atomic gas. The correlations of Σ_{dust} with Σ_{H_2} or with Σ_{gas}

have the strongest significance and hold for individual galaxies as well as for the whole sample.

- The scaling relations are marginally dependent on galaxy properties. The mean dust-to-gas mass ratio varies across our sample with each galaxy showing local enhancements. Molecular fractions increase as Σ_{dust} and Σ_{star} increase.
- The atomic gas mass surface density for each galaxy is in a restricted range that varies from galaxy to galaxy and is related to the column density that the gas needs to shield the molecular phase. Galaxies with a higher dust-to-gas mass ratio need a lower column density of HI to provide the shielding, with local variations related to the Σ_{star} .
- The $A_{V,BD}$ and the $A_{V,SED}^{young}$ that we estimated through SED fitting are in very good agreement, with 88.6% of our data points differing by less than 0.5 dex. $A_{V,SED}^{young}$ inferred by CIGALE could serve as a tracer of the attenuation in larger samples, where IFU observations might be more expensive and time-consuming.
- We estimate the ratio of the $A_{V,BD}$ over the total stellar $A_{V,SED}$, for star-forming regions, to be equal to 0.59 ± 0.05 , slightly larger than the one found in previous studies.
- Both $A_{V,BD}$ and $A_{V,SED}^{young}$ are affected by a combination of a screen dust component and a mixture of dust and emitting material. On the contrary, $A_{V,SED}^{old}$ as a function of the Σ_{dust} follows the models where sources and dust are mixed (either the slab or the sandwich model).

Data availability

The maps of the derived properties that were used for the main results (see Figs. 2, 4, 5, 6, 7) are available at the CDS via <https://cdsarc.cds.unistra.fr/viz-bin/cat/J/A+A/702/A264>

Acknowledgements. We are grateful to the anonymous referee for a constructive report that improved the quality of the manuscript. We would like to thank Adam Leroy and Francesco Belfiore for productive discussions on this project and on the use of PHANGS-MUSE data. We acknowledge financial support from: PRIN MIUR 2017 – 20173ML3WW_001; INAF mainstream 2018 program “Gas-DustPedia: A definitive view of the ISM in the Local Universe”; INAF-Mini Grant 2024 program “Dust emission and optical extinction as gas

tracers in star forming galaxies”. DustPedia is a collaborative focused research project supported by the European Union under the Seventh Framework Programme (2007–2013) call (proposal no. 606824). The participating institutions are: Cardiff University, UK; National Observatory of Athens, Greece; Ghent University, Belgium; Université Paris-Sud, France; National Institute for Astrophysics, Italy and CEA (Paris), France. This work made use of THINGS, “The H_I Nearby Galaxy Survey” (Walter et al. 2008) and HERACLES, “The HERA CO-Line Extragalactic Survey” (Leroy et al. 2009). This research made use of Astropy: a community-developed core Python package and an ecosystem of tools and resources for astronomy (Astropy Collaboration 2013, 2018, 2022, <http://www.astropy.org>); matplotlib, a Python library for publication quality graphics (Hunter 2007); NumPy (Harris et al. 2020); SciPy (Virtanen et al. 2020); TOPCAT, an interactive graphical viewer and editor for tabular data (Taylor 2005); Photutils, an Astropy package for detection and photometry of astronomical sources (Bradley et al. 2024).

References

- Abdo, A. A., Ackermann, M., Ajello, M., et al. 2010, *ApJ*, 710, 133
- Abdurro’uf, Lin, Y. T., Hirashita, H., et al. 2022, *ApJ*, 935, 98
- Abramson, A., Kenney, J. D. P., Crowl, H. H., et al. 2011, *AJ*, 141, 164
- Amorín, R., Muñoz-Tuñón, C., Aguerri, J. A. L., & Planesas, P. 2016, *A&A*, 588, A23
- Anand, G. S., Lee, J. C., Van Dyk, S. D., et al. 2021, *MNRAS*, 501, 3621
- Aniano, G., Draine, B. T., Gordon, K. D., & Sandstrom, K. 2011, *PASP*, 123, 1218
- Astropy Collaboration (Robitaille, T. P., et al.) 2013, *A&A*, 558, A33
- Astropy Collaboration (Price-Whelan, A. M., et al.) 2018, *AJ*, 156, 123
- Astropy Collaboration (Price-Whelan, A. M., et al.) 2022, *ApJ*, 935, 167
- Barrera-Ballesteros, J. K., Utomo, D., Bolatto, A. D., et al. 2020, *MNRAS*, 492, 2651
- Battisti, A., Shivaee, I., Park, H. J., et al. 2025, *PASA*, 42, e022
- Bianchi, S. 2007, *A&A*, 471, 765
- Bianchi, S. 2008, *A&A*, 490, 461
- Bolatto, A. D., Wolfire, M., & Leroy, A. K. 2013, *ARA&A*, 51, 207
- Boquien, M., Buat, V., Boselli, A., et al. 2012, *A&A*, 539, A145
- Boquien, M., Boselli, A., Buat, V., et al. 2013, *A&A*, 554, A14
- Boquien, M., Kennicutt, R., Calzetti, D., et al. 2016, *A&A*, 591, A6
- Boquien, M., Burgarella, D., Roehlly, Y., et al. 2019, *A&A*, 622, A103
- Bradley, L., Sipőcz, B., Robitaille, T., et al. 2024, <https://doi.org/10.5281/zenodo.13989456>
- Brazzini, M., Belfiore, F., Ginolfi, M., et al. 2024, *A&A*, 691, A173
- Brinchmann, J., Charlot, S., Kauffmann, G., et al. 2013, *MNRAS*, 432, 2112
- Bruzual, G., & Charlot, S. 2003, *MNRAS*, 344, 1000
- Buat, V., Noll, S., Burgarella, D., et al. 2012, *A&A*, 545, A141
- Buat, V., Mountrichas, G., Yang, G., et al. 2021, *A&A*, 654, A93
- Buchner, J. 2016, *Stat. Comput.*, 26, 383
- Buchner, J. 2019, *PASP*, 131, 108005
- Buchner, J. 2021, *J. Open Source Softw.*, 6, 3001
- Calzetti, D., Kinney, A. L., & Storchi-Bergmann, T. 1994, *ApJ*, 429, 582
- Calzetti, D., Armus, L., Bohlin, R. C., et al. 2000, *ApJ*, 533, 682
- Cardelli, J. A., Clayton, G. C., & Mathis, J. S. 1989, *ApJ*, 345, 245
- Casasola, V., Cassarà, L. P., Bianchi, S., et al. 2017, *A&A*, 605, A18
- Casasola, V., Bianchi, S., De Vis, P., et al. 2020, *A&A*, 633, A100
- Casasola, V., Bianchi, S., Magrini, L., et al. 2022, *A&A*, 668, A130
- Catinella, B., Haynes, M. P., Giovanelli, R., Gardner, J. P., & Connolly, A. J. 2008, *ApJ*, 685, L13
- Chakraborty, A., Kundu, M., Chatterjee, S., et al. 2025, *A&A*, 694, A140
- Chastenet, J., De Looze, I., Relaño, M., et al. 2024, *A&A*, 690, A348
- Chiang, I.-D., Sandstrom, K. M., Chastenet, J., et al. 2024, *ApJ*, 964, 18
- Chung, A., van Gorkom, J. H., Kenney, J. D. P., Crowl, H., & Vollmer, B. 2009, *AJ*, 138, 1741
- Ciesla, L., Charmandaris, V., Georgakakis, A., et al. 2015, *A&A*, 576, A10
- Clark, C. J. R., Verstocken, S., Bianchi, S., et al. 2018, *A&A*, 609, A37
- Concas, A., & Popesso, P. 2019, *MNRAS*, 486, L91
- Corbelli, E., Bianchi, S., Cortese, L., et al. 2012, *A&A*, 542, A32
- Cormier, D., Bigiel, F., Jiménez-Donaire, M. J., et al. 2018, *MNRAS*, 475, 3909
- Cutri, R. M., Skrutskie, M. F., van Dyk, S., et al. 2003, *VizieR On-line Data Catalog: II/246*
- Dame, T. M., Hartmann, D., & Thaddeus, P. 2001, *ApJ*, 547, 792
- Davies, J. I., Nersesian, A., Baes, M., et al. 2019, *A&A*, 626, A63
- De Geyter, G., Baes, M., Fritz, J., & Camps, P. 2013, *A&A*, 550, A74
- den Brok, J. S., Chatzigiannakis, D., Bigiel, F., et al. 2021, *MNRAS*, 504, 3221
- Disney, M., Davies, J., & Phillipps, S. 1989, *MNRAS*, 239, 939
- Draine, B. T., Dale, D. A., Bendo, G., et al. 2007, *ApJ*, 663, 866
- Eisenstein, D. J., Weinberg, D. H., Agol, E., et al. 2011, *AJ*, 142, 72
- Emsellem, E., Schinnerer, E., Santoro, F., et al. 2022, *A&A*, 659, A191
- Farley, B., Ahmed, U. T., Hopkins, A., et al. 2025, *PASA*, 42
- Fazio, G. G., Hora, J. L., Allen, L. E., et al. 2004, *ApJS*, 154, 10
- Fitzpatrick, E. L. 1999, *PASP*, 111, 63
- Foyle, K., Wilson, C. D., Mentuch, E., et al. 2012, *MNRAS*, 421, 2917
- Gil de Paz, A., Boissier, S., Madore, B. F., et al. 2007, *ApJS*, 173, 185
- Griffin, M. J., Abergel, A., Abreu, A., et al. 2010, *A&A*, 518, L3
- Grossi, M., Corbelli, E., Bizzocchi, L., et al. 2016, *A&A*, 590, A27
- Harris, C. R., Millman, K. J., van der Walt, S. J., et al. 2020, *Nature*, 585, 357
- Hensley, B. S., & Draine, B. T. 2021, *ApJ*, 906, 73
- Hughes, T. M., Baes, M., Fritz, J., et al. 2014, *A&A*, 565, A4
- Hummer, D. G., & Storey, P. J. 1987, *MNRAS*, 224, 801
- Hunter, J. D. 2007, *Comput. Sci. Eng.*, 9, 90
- Israel, F. P. 2020, *A&A*, 635, A131
- Jones, A. P., Köhler, M., Ysard, N., Bocchio, M., & Verstraete, L. 2017, *A&A*, 602, A46
- Kouroumpatzakis, K., Zezas, A., Maragkoudakis, A., et al. 2021, *MNRAS*, 506, 3079
- Koutoulidis, L., Mountrichas, G., Georgantopoulos, I., Pouliaxis, E., & Plionis, M. 2022, *A&A*, 658, A35
- Kovačić, I., Barnes, A. T., Bigiel, F., et al. 2025, *A&A*, 694, A87
- Kreckel, K., Groves, B., Schinnerer, E., et al. 2013, *ApJ*, 771, 62
- Leitherer, C., Li, I. H., Calzetti, D., & Heckman, T. M. 2002, *ApJS*, 140, 303
- Leroy, A. K., Walter, F., Brinks, E., et al. 2008, *AJ*, 136, 2782
- Leroy, A. K., Walter, F., Bigiel, F., et al. 2009, *AJ*, 137, 4670
- Leroy, A. K., Bigiel, F., de Blok, W. J. G., et al. 2012, *AJ*, 144, 3
- Leroy, A. K., Schinnerer, E., Hughes, A., et al. 2021, *ApJS*, 257, 43
- Leroy, A. K., Rosolowsky, E., Usero, A., et al. 2022, *ApJ*, 927, 149
- Martin, D. C., Fanson, J., Schiminovich, D., et al. 2005, *ApJ*, 619, L1
- Momcheva, I. G., Lee, J. C., Ly, C., et al. 2013, *AJ*, 145, 47
- Morrissey, P., Conrow, T., Barlow, T. A., et al. 2007, *ApJS*, 173, 682
- Mountrichas, G., Masoura, V. A., Xilouris, E. M., et al. 2022, *A&A*, 661, A108
- Muñoz-Mateos, J. C., Gil de Paz, A., Boissier, S., et al. 2009, *ApJ*, 701, 1965
- Nersesian, A., Xilouris, E. M., Bianchi, S., et al. 2019, *A&A*, 624, A80
- Noll, S., Burgarella, D., Giovannoli, E., et al. 2009, *A&A*, 507, 1793
- Orellana, G., Nagar, N. M., Elbaz, D., et al. 2017, *A&A*, 602, A68
- Osterbrock, D. E., & Ferland, G. J. 2006, *Astrophysics of Gaseous Nebulae and Active Galactic Nuclei* (Sausalito, CA: University Science Books)
- Paspaliaris, E. D., Xilouris, E. M., Nersesian, A., et al. 2021, *A&A*, 649, A137
- Paspaliaris, E. D., Xilouris, E. M., Nersesian, A., et al. 2023, *A&A*, 669, A11
- Pilbratt, G. L., Riedinger, J. R., Passvogel, T., et al. 2010, *A&A*, 518, L1
- Piotrowska, J. M., Bluck, A. F. L., Maiolino, R., Concas, A., & Peng, Y. 2020, *MNRAS*, 492, L6
- Poglitich, A., Waelkens, C., Geis, N., et al. 2010, *A&A*, 518, L2
- Rieke, G. H., Young, E. T., Engelbracht, C. W., et al. 2004, *ApJS*, 154, 25
- Roehlly, Y., Burgarella, D., Buat, V., et al. 2014, in *Astronomical Data Analysis Software and Systems XXIII*, eds. N. Manset, & P. Forshay, *Astronomical Society of the Pacific Conference Series*, 485, 347
- Salpeter, E. E. 1955, *ApJ*, 121, 161
- Salvestrini, F., Bianchi, S., & Corbelli, E. 2025, *A&A*, 699, A346
- Sandstrom, K. M., Leroy, A. K., Walter, F., et al. 2013, *ApJ*, 777, 5
- Schlafly, E. F., & Finkbeiner, D. P. 2011, *ApJ*, 737, 103
- Schruba, A., Leroy, A. K., Walter, F., et al. 2011, *AJ*, 142, 37
- Shetty, R., Glover, S. C., Dullemond, C. P., et al. 2011, *MNRAS*, 415, 3253
- Skrutskie, M. F., Cutri, R. M., Stiening, R., et al. 2006, *AJ*, 131, 1163
- Strong, A. W., & Mattox, J. R. 1996, *A&A*, 308, L21
- Taylor, M. B. 2005, in *Astronomical Data Analysis Software and Systems XIV*, eds. P. Shopbell, M. Britton, & R. Ebert, *Astronomical Society of the Pacific Conference Series*, 347, 29
- Teng, Y.-H., Sandstrom, K. M., Sun, J., et al. 2022, *ApJ*, 925, 72
- Tody, D. 1986, in *Instrumentation in Astronomy VI*, ed. D. L. Crawford, *Society of Photo-Optical Instrumentation Engineers (SPIE) Conference Series*, 627, 733
- Tody, D. 1993, in *Astronomical Data Analysis Software and Systems II*, eds. R. J. Hanisch, R. J. V. Brissenden, & J. Barnes, *Astronomical Society of the Pacific Conference Series*, 52, 173
- van Dishoeck, E. F., & Black, J. H. 1988, *ApJ*, 334, 771
- Verheijen, M., Deshev, B., van Gorkom, J., et al. 2010, arXiv e-prints [arXiv:1009.0279]
- Virtanen, P., Gommers, R., Oliphant, T. E., et al. 2020, *Nat. Methods*, 17, 261
- Walter, F., Brinks, E., de Blok, W. J. G., et al. 2008, *AJ*, 136, 2563
- Werner, M. W., Roellig, T. L., Low, F. J., et al. 2004, *ApJS*, 154, 1
- Weżgowiec, M., Soida, M., & Bomans, D. J. 2012, *A&A*, 544, A113
- Wong, T., & Blitz, L. 2002, *ApJ*, 569, 157
- Wright, E. L., Eisenhardt, P. R. M., Mainzer, A. K., et al. 2010, *AJ*, 140, 1868
- Xilouris, E. M., Byun, Y. I., Kylafis, N. D., Paleologou, E. V., & Papamastorakis, J. 1999, *A&A*, 344, 868
- Yajima, Y., Sorai, K., Miyamoto, Y., et al. 2021, *PASJ*, 73, 257
- York, D. G., Adelman, J., Anderson, J. E., Jr., et al. 2000, *AJ*, 120, 1579

Appendix A: Maps of galaxies' properties

In this Appendix we show maps of the resolved properties of galaxies in our sample, at a resolution of 18".

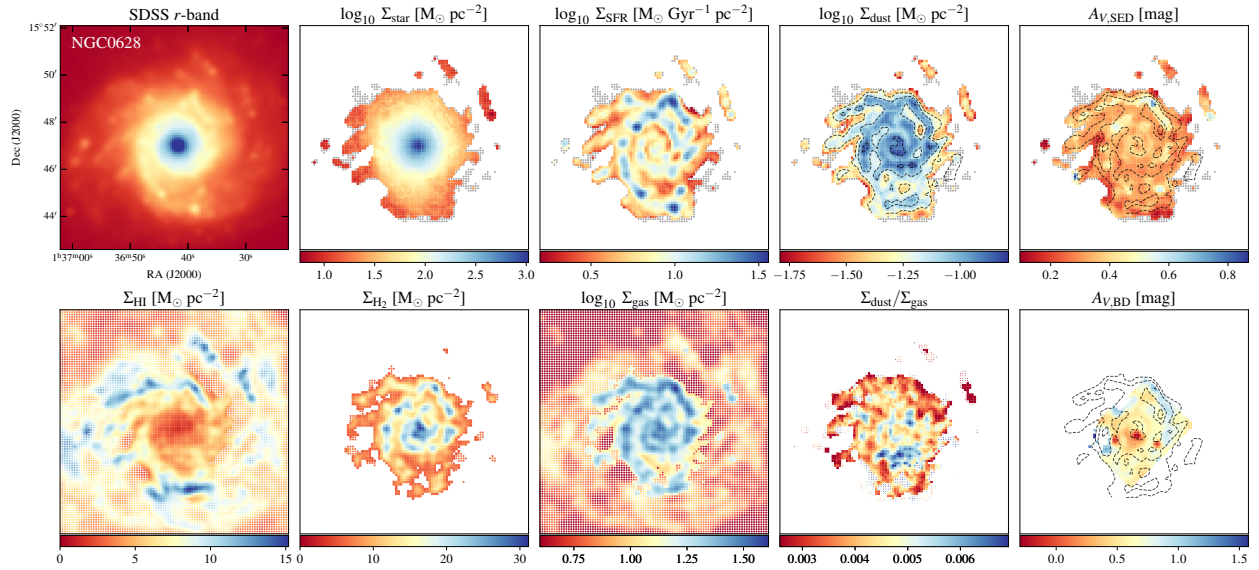


Fig. A.1. Maps of observed and derived properties of NGC 0628. *Top*: Convolved and re-gridded SDSS r band, $\log_{10} \Sigma_{\text{star}}$, $\log_{10} \Sigma_{\text{SFR}}$, $\log_{10} \Sigma_{\text{dust}}$, as well as SED-fitting-derived V-band attenuation ($A_{V,\text{SED}}$), from left to right. *Bottom*: Σ_{HI} , Σ_{H_2} , $\log_{10} \Sigma_{\text{gas}}$, DGR and V-band attenuation derived by the BD ($A_{V,\text{BD}}$), from left to right. Grey points correspond to pixels that are rejected (see Sec. 2.1.1, 2.3 for more details). The Σ_{HI} and Σ_{H_2} maps extend up to their corresponding 3σ limit. For Σ_{HI} , Σ_{H_2} and $A_{V,\text{BD}}$ maps pixels that correspond to areas excluded by the SED-fitting analysis are plotted with smaller dots. In $\log_{10} \Sigma_{\text{gas}}$ map, pixels excluded by the SED-fitting analysis and having both HI and CO detection are depicted by smaller squares, while pixels with only HI and not CO are plotted with dots. Contours plotted in some map are from $\log_{10} \Sigma_{\text{dust}}$ [$M_{\odot} \text{pc}^{-2}$] maps with a lowest contour at -1.3 and linear spacing with the highest at -0.9. Dots in each map indicate areas excluded from the SED fitting routine.

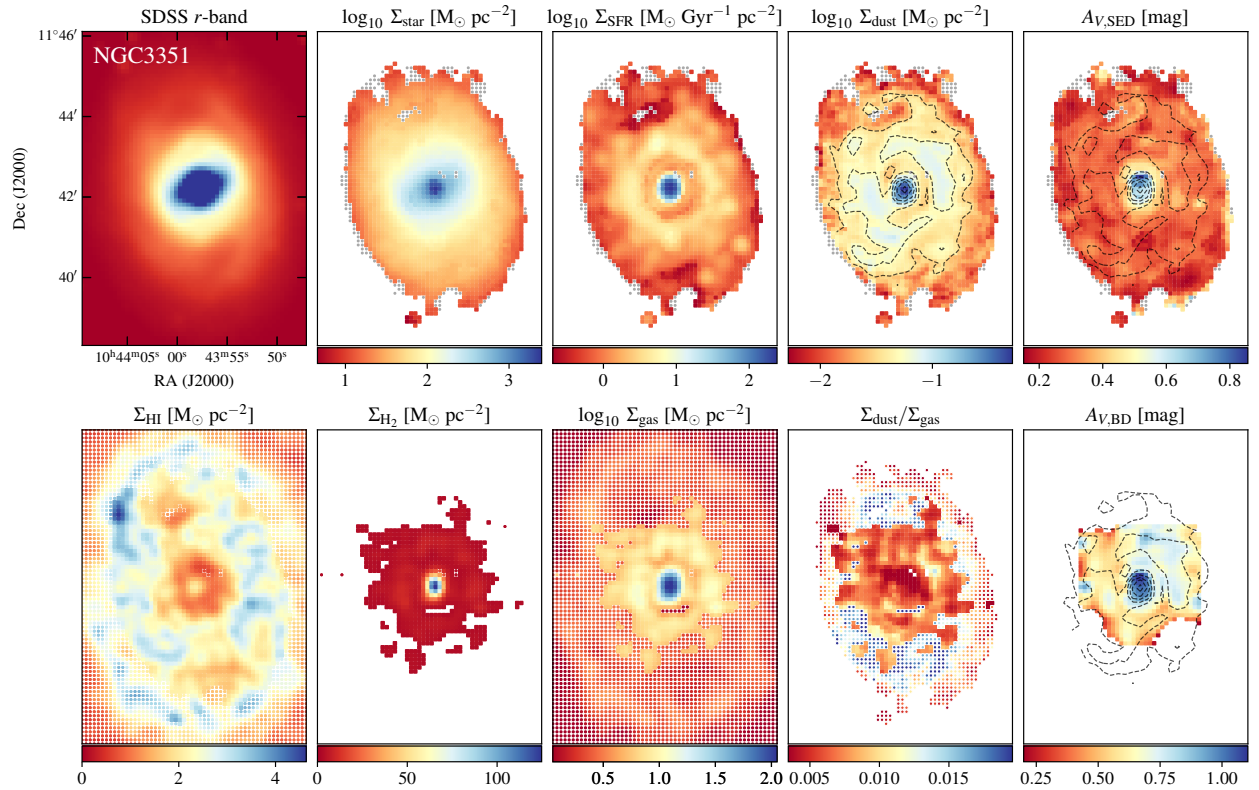


Fig. A.2. Same as Fig. A.1, but for NGC 3351. Contours are taken from the $\log_{10} \Sigma_{\text{dust}}$ [$M_{\odot} \text{pc}^{-2}$] maps with a lowest contour at -1.5 and linear spacing with the highest at 0.

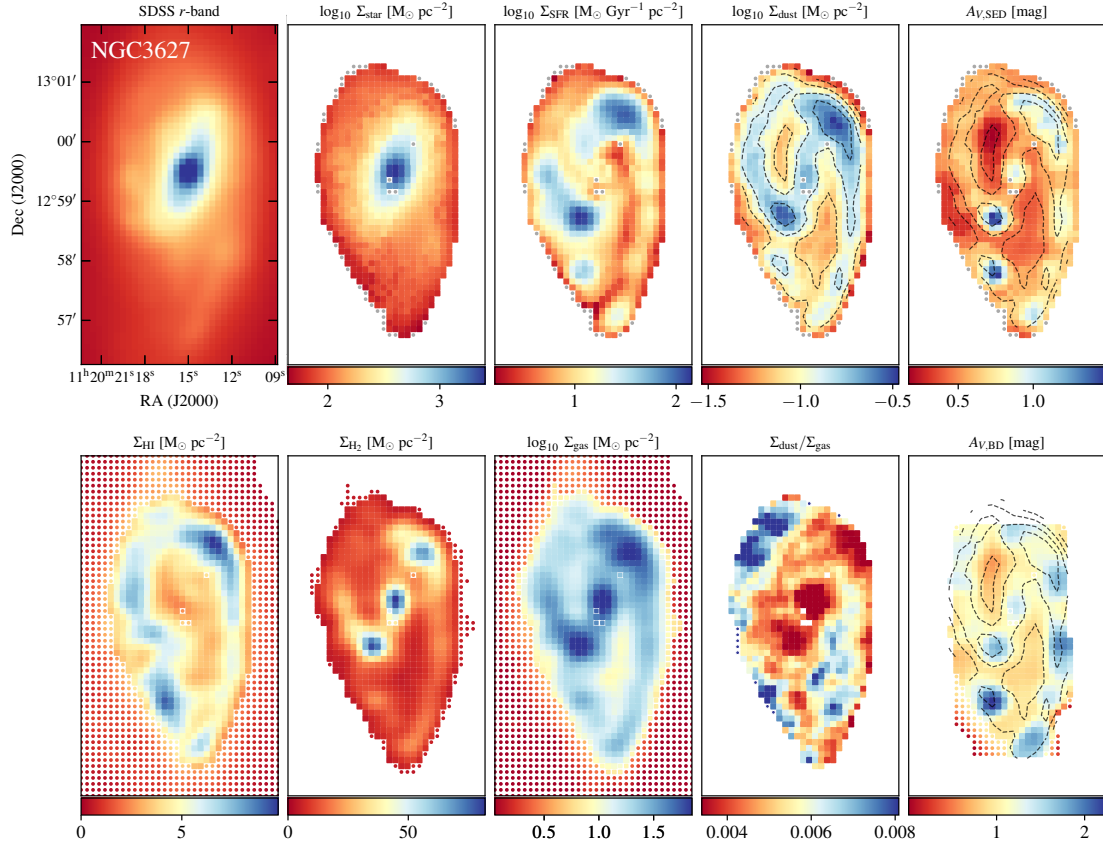


Fig. A.3. Same as Fig. A.1, but for NGC 3627. Contours are taken from the $\log_{10} \Sigma_{\text{dust}} [\text{M}_{\odot} \text{pc}^{-2}]$ maps with a lowest contour at -1.5 and linear spacing with the highest at -0.7.

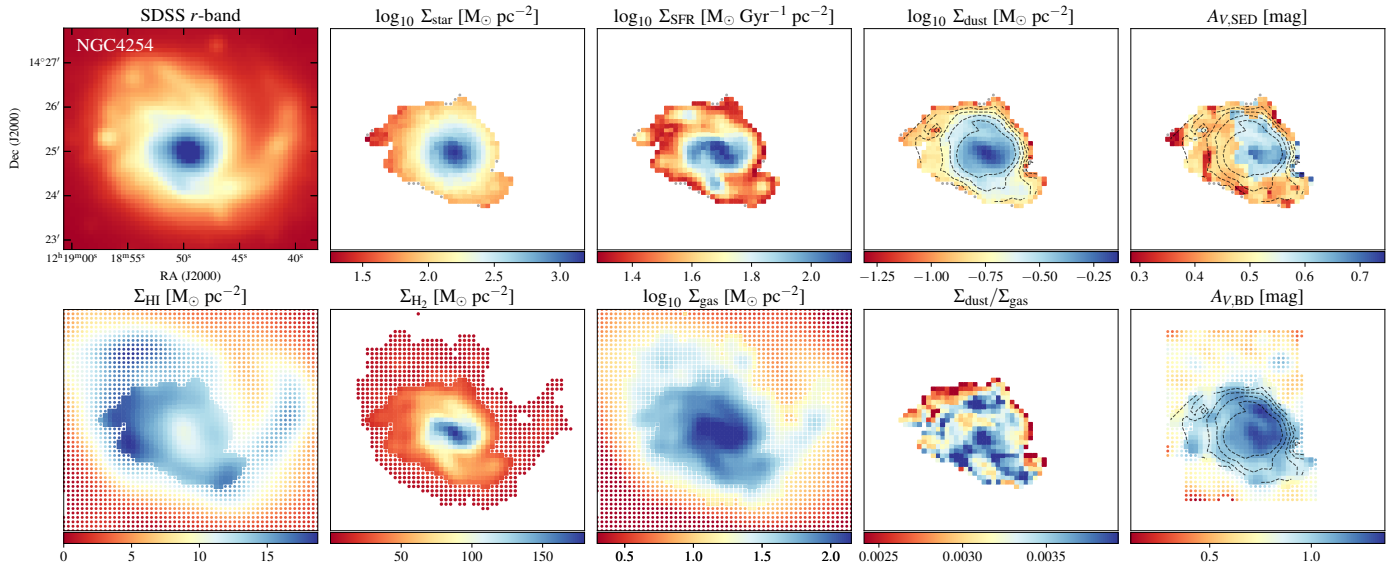


Fig. A.4. Same as Fig. A.1, but for NGC 4254. Contours are taken from the $\log_{10} \Sigma_{\text{dust}} [\text{M}_{\odot} \text{pc}^{-2}]$ maps with a lowest contour at -1.1 and linear spacing with the highest at -0.5.

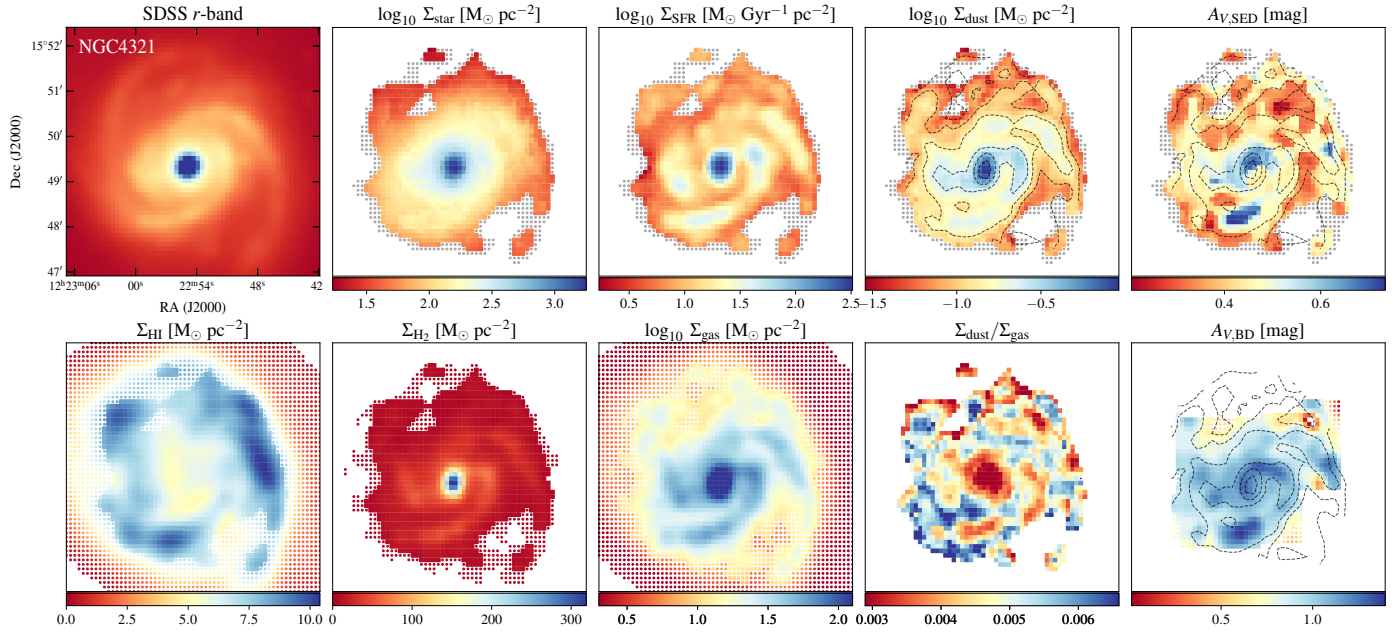


Fig. A.5. Same as Fig. A.1, but for NGC 4321. Contours are taken from the $\log_{10} \Sigma_{\text{dust}} [\text{M}_{\odot} \text{pc}^{-2}]$ maps with a lowest contour at -1.5 and linear spacing with the highest at 0.

Appendix B: CO-to-H₂ conversion factor α_{CO} and CO(2-1)-to-CO(1-0) line ratio R_{21}

In this appendix, we discuss our assumptions to infer the molecular gas surface density from ¹²CO J=2-1 line maps and possible dependencies of our results from these assumptions. As stated in the main paper we used a MW-disc CO-to-H₂ conversion factor $\alpha_{\text{CO}} = 4.4 \text{ M}_{\odot} \text{pc}^{-2} (\text{K km s}^{-1})^{-1}$ (Bolatto et al. 2013) and an intrinsic line ratio $R_{21} = I_{\text{CO}(2-1)} / I_{\text{CO}(1-0)} = 0.7$ (e.g. Leroy et al. 2009; Schruba et al. 2011). Although these values have been widely used by previous studies of the ISM in nearby galaxies (e.g. Casasola et al. 2017), variations in these two parameters are possible due to variations in local ISM conditions in clouds, such as metallicity, temperature, mass surface density, velocity dispersion, and optical thickness. The metallicity dependencies of α_{CO} have been studied by many authors (e.g. Amorín et al. 2016) but for our sample metallicities are very close to solar (Brazzini et al. 2024) and we do not expect significant deviations from the assumed value across the bright discs we investigate. Other studies have found α_{CO} to deviate from the typical MW in galaxy’s central regions (e.g. Israel 2020; Teng et al. 2022).

Dedicated surveys for accurate determination of α_{CO} often include galaxies of our sample, such as the CO-isotopologue investigation by Cormier et al. (2018) or the dust based studies by Sandstrom et al. (2013) and Chiang et al. (2024). The usage of CO isotopologues as tracers of molecular mass primarily traces dense gas, leading to underestimation of the total molecular mass, given the presence of diffuse molecular gas in the ISM. Sandstrom et al. (2013) used the dust as gas tracer and the gas-to-dust ratio to infer α_{CO} in kiloparsec-scale regions. They found an average α_{CO} radial profile that is generally flat, with a depression towards the centre, particularly evident for NGC 3351, NGC 3627 and NGC 4321 ($R < 0.1R_{25}$). In the same area, the α_{CO} was found significantly increased in NGC 4254. They provided average I_{CO} -weighted values for each galaxy and as optimal average α_{CO} for the whole sample, $3.1 \text{ M}_{\odot} \text{pc}^{-2} (\text{K km s}^{-1})^{-1}$. Chiang et al. (2024) using a similar method, studies the variation in α_{CO} as a function of several physical quantities, and find negative anti-correlations with SFR, radiation field intensity, CO intensity and galactocentric distance.

Galaxies in our sample have also been targets for R_{21} investigations. Although these are also discussed by Sandstrom et al. (2013), we use the data of more recent and dedicated surveys, which give resulting values more consistent between each other and with our assumed ratio (den Brok et al. 2021; Yajima et al. 2021; Leroy et al. 2022). These works find R_{21} in the range of 0.45 – 0.83 as average values across the disc of galaxies in our sample. The mean of the three values (two only for NGC 3351) reported for each galaxy by den Brok et al. (2021), Yajima et al. (2021) and by Leroy et al. (2022) are 0.56, 0.67, 0.50, 0.69, 0.72 for NGC 0628, NGC 3351, NGC 3627, NGC 4254, and NGC 4321, respectively. These are within 30% of our assumed R_{21} ratio, with NGC 4254 and NGC 4321 fully consistent with our assumed R_{21} ratio. There are no significant radial variations measured for the region of interest in galaxies of our sample. Only for NGC 3627 and NGC 4321 the ALMA observations analysed by den Brok et al. (2021) show a positive radial gradient or a factor 1.5 enhancement in the centre, respectively. These radial variations are not however confirmed by other observations such as HERACLES (IRAM-30m) data. We notice that for NGC 3627 and NGC 4321 results of different analyses give somewhat different mean values. Because of these discrepancies we have considered a uniform $R_{21} = 0.7$ ratio in the present study.

With the aim to verify if our results are significantly affected by variations in α_{CO} and R_{21} with respect to the assumed values, in Fig. B.1 we plot the f_{H_2} as a function of the DGR for four different cases. In the top row, we assume the typical $\alpha_{\text{CO}} = 4.4 \text{ M}_{\odot} \text{pc}^{-2} (\text{K km s}^{-1})^{-1}$ as in the rest of the paper (same as Fig. 4 but with a common x-axis range for all galaxies); in the second row, the average α_{CO} values found by Sandstrom et al. (2013) for each galaxy with a constant R_{21} has been used; in the third row, we set $\alpha_{\text{CO}} = 4.4 \text{ M}_{\odot} \text{pc}^{-2} (\text{K km s}^{-1})^{-1}$ and use $R_{21} = 0.56, 0.67, 0.50, 0.69, 0.72$ for NGC 0628, NGC 3351, NGC 3627, NGC 4254, and NGC 4321, respectively. In addition, for NGC 3351, NGC 3627, and NGC 4321 we use a 1.5 enhancement factor in R_{21} and a factor

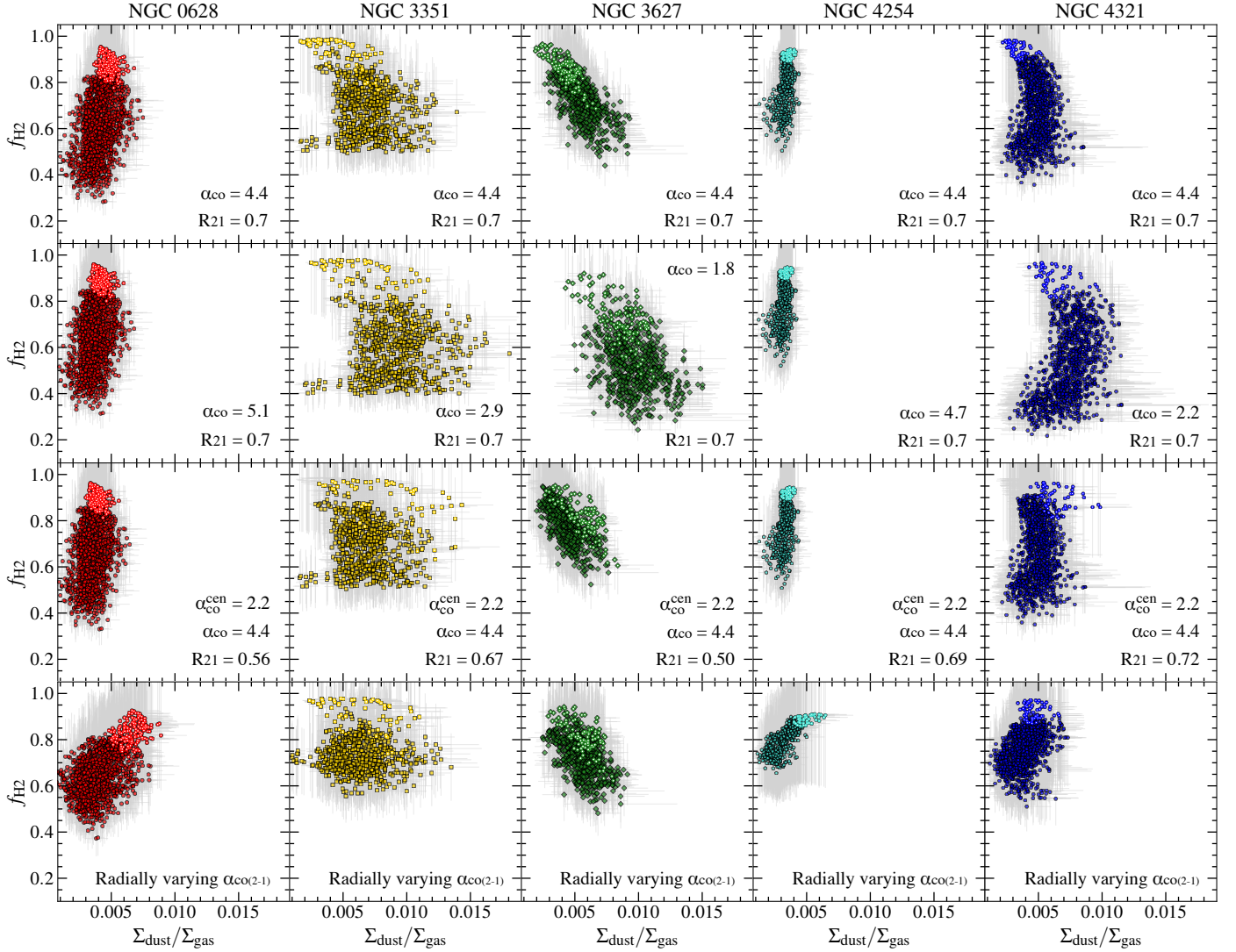


Fig. B.1. Molecular gas mass fraction as a function dust-to-gas mass ratio, for each galaxy in the sample. The molecular gas is estimated assuming a constant MW $\alpha_{\text{CO}} = 4.4 \text{ M}_{\odot} \text{ pc}^{-2} (\text{K km s}^{-1})^{-1}$ (Bolatto et al. 2013 and $R_{21}=0.7$ (top panels), a radially constant α_{CO} which varies from galaxy to galaxy as found by Sandstrom et al. (2013) (middle-top panels), a constant $\alpha_{\text{CO}} = 4.4 \text{ M}_{\odot} \text{ pc}^{-2} (\text{K km s}^{-1})^{-1}$ throughout the galaxies except in the central areas, and a radially constant R_{21} value varying from galaxy to galaxy (den Brok et al. 2021; Yajima et al. 2021; Leroy et al. 2022, middle-bottom panels), and a radially varying $\alpha_{\text{CO}(2-1)}$ as found by Chiang et al. (2024, bottom panels). The α_{CO} and R_{21} values used for each panel are shown in the lower right corners. Pixels within the inner $0.15 R_{25}$ area are plotted with open symbols. Uncertainties are shown with grey error bars.

2 decrease in α_{CO} for the central region; finally, in the bottom row, we use the correlation found by Chiang et al. (2024) between $\alpha_{\text{CO}(2-1)}$ and galactocentric distance (with no need to correct for R_{21}). The pixels that lie in the $R < 0.15 R_{25}$ areas are plotted with open symbols.

The main conclusion of our investigation in this Appendix is that by changing our assumptions on R_{21} and on α_{CO} we recover similar DGR trends across the galaxies and from one galaxy to another. Although molecular fractions change, these always increase with the DGR for NGC 0628 and NGC 4254. If we exclude the central area, for which the CO-to- H_2 conversion factor can be lower than what has been shown in Fig. B.1, NGC 3351 and NGC 4321 have no correlation between the molecular fraction and the DGR where the molecular phase dominates, while NGC 3627 shows a decreasing DGR as the molecular fraction increases. NGC 4321 shows a decrease in the dust abundance on the outskirts, under all assumptions apart from the case of the radially dependent α_{CO} by Chiang et al. (2024). In this case the main part of the disc shows a mild positive correlation, with some deviation for outskirts and centre. In an increasing order we list the average DGRs found in the sampled regions: 0.0033 ± 0.0005 , 0.0041 ± 0.001 , 0.0048 ± 0.0010 , 0.0054 ± 0.0013 and 0.0069 ± 0.0020 , for NGC 4254, NGC 0628, NGC 4321, NGC 3627, and NGC 3351, respectively, using the standard values as in the main paper. These values increase by decreasing α_{CO} but the sequence is unchanged; also when using the Chiang et al. 2024 α_{CO} prescription, with the only exception of NGC 4321 which in this case has a DGR equal to 0.0039 ± 0.001 and is second in increasing order, instead of being third (see Sec. 3.2).

We have also estimated the best-fit parameters and the correlation coefficients for the $\log_{10} \Sigma_{\text{dust}} - \log_{10} \Sigma_{\text{H}_2}$ and $\log_{10} \Sigma_{\text{dust}} - \log_{10} \Sigma_{\text{gas}}$ relations for various α_{CO} and R_{21} and we do not find significant differences. For instance, if we use the Chiang et al. (2024) prescription where α_{CO} changes with galactocentric distance, the correlations of $\log_{10} \Sigma_{\text{dust}}$ with $\log_{10} \Sigma_{\text{H}_2}$ and $\log_{10} \Sigma_{\text{gas}}$,

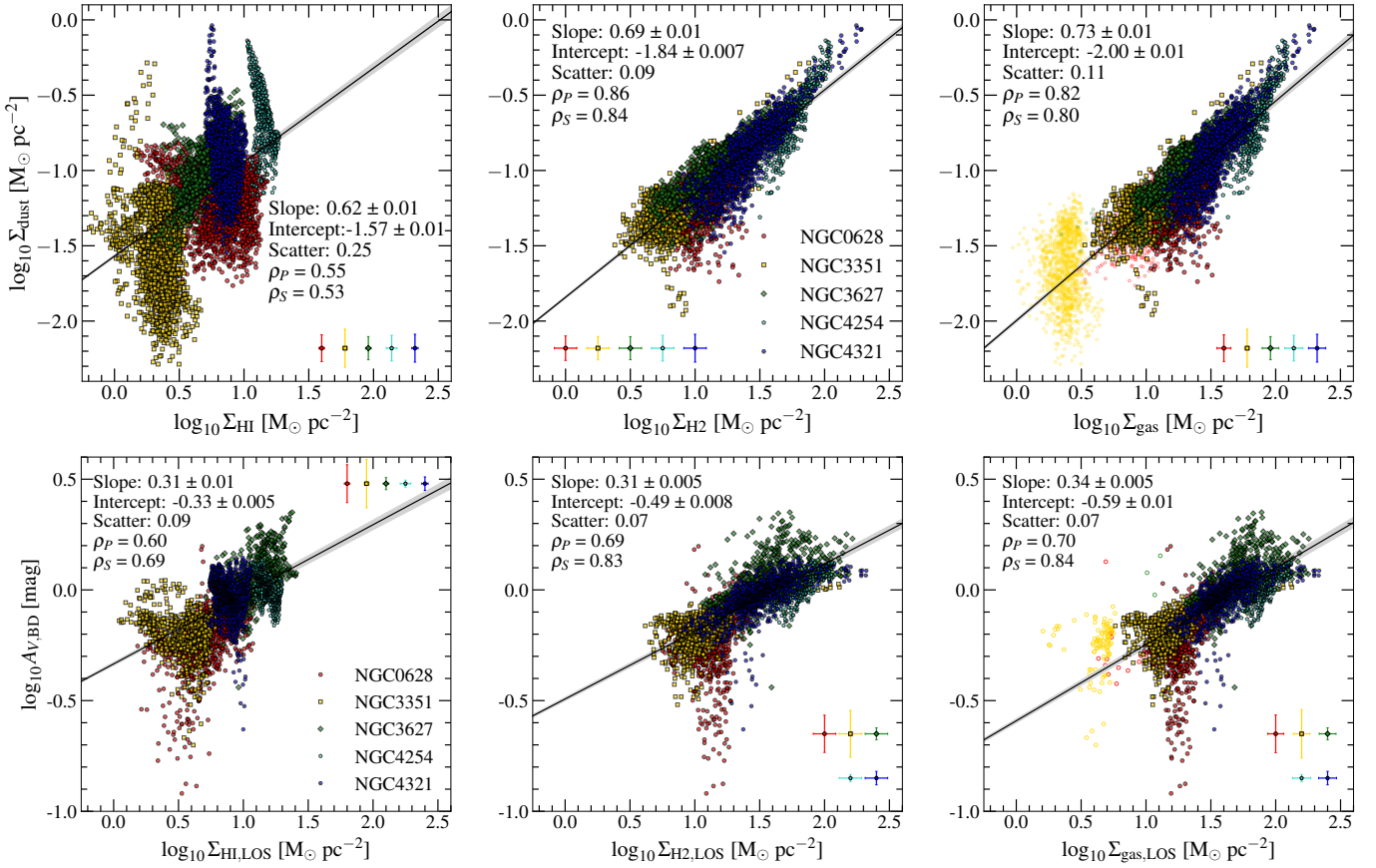


Fig. B.2. *Top panels*, same as in Fig. 2 and *bottom panels* same as in Fig. 5, but with using the Chiang et al. (2024) prescription for a radially varying α_{CO} (see text for details.)

as well as $\log_{10} A_{V,BD}$ with $\log_{10} \Sigma_{H_2}$ and $\log_{10} \Sigma_{gas}$, have similar slopes, scatter and correlation significance to those found using a constant α_{CO} (see Fig. B.2). We prefer to use the constant α_{CO} values in the main paper to avoid any possible influence of circular reasoning: in fact the Chiang et al. (2024) prescription is found assuming that the total gas surface density is traced by the dust surface density given a constant gas-to-metal ratio. Thus we would study the correlation of Σ_{dust} with a quantity that has been derived using Σ_{dust} (though assuming a different dust model than ours, as in Chiang et al. 2024). Nevertheless, similar correlations (not shown here) are found also using the Bolatto et al. (2013) formula that accounts for a decrease in α_{CO} in denser regions (see their Eq. 31). This is recovered using several methodologies and not only using dust as a proxy of gas. In any case, the α_{CO} variations mostly affect central areas, which are only a small portion of the discs we investigate, and do not affect our main conclusions.

Appendix C: Attenuations for simple geometries

For a homogeneously mixed thin layer of dust and sources, of optical depth τ_λ perpendicular to the layer, the radiative transfer solution can be derived analytically in the absence of scattering: it is the slab model (Disney et al. 1989) and the corresponding attenuation can be written as

$$A_\lambda = -2.5 \log_{10} \frac{I}{I_0} = -2.5 \log_{10} \frac{1 - e^{-\tau_\lambda}}{\tau_\lambda}, \quad (\text{C.1})$$

where, for simplicity, we consider only the line of sight perpendicular to the layer (face-on view). For $\tau_\lambda \rightarrow 0$, Eq. C.1 can be written using series expansion as

$$A_\lambda = 1.086 \frac{\tau_\lambda}{2}. \quad (\text{C.2})$$

Instead, for $\tau \rightarrow \infty$, it is

$$A_\lambda = 2.5 \log_{10} \tau_\lambda. \quad (\text{C.3})$$

Using these limits, $\tau_\lambda = k(\lambda)\tau_V$ with $k(\lambda)$ the (V-band normalised) extinction law, and Eq. 3, rewritten as

$$A_{V,BD} = \frac{A_{H\beta} - A_{H\alpha}}{k(H\beta) - k(H\alpha)}, \quad (\text{C.4})$$

we can easily find that $A_{V,BD}$ tends to A_V for low optical depths, and to the constant value $2.5 \log_{10}(k(H\beta)/k(H\alpha))/(k(H\beta) - k(H\alpha))$ at high optical depths. This is shown in Fig. C.1, where we plot $A_{V,BD}$ vs A_V for a slab using the extinction law of the THEMIS dust model ($k(H\alpha) = 0.81$, $k(H\beta) = 1.14$).

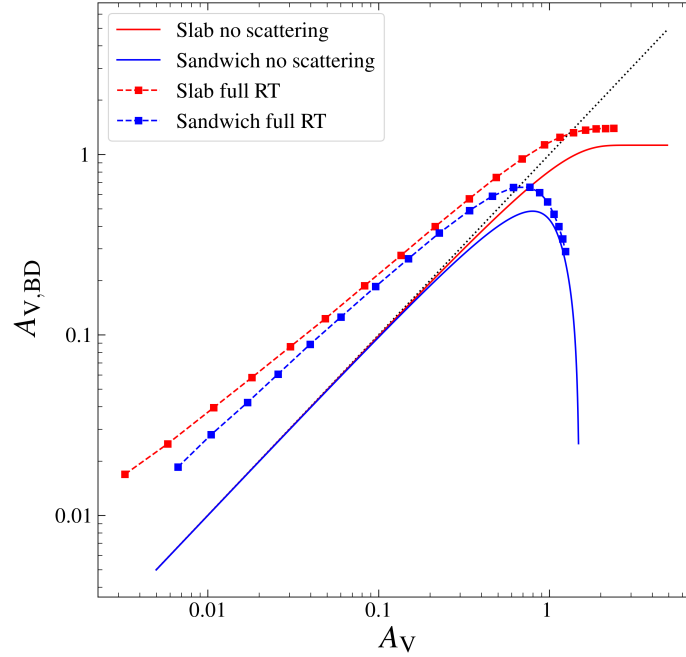


Fig. C.1. $A_{V,BD}$ vs A_V for the models discussed in the text. The dotted line shows the 1-to-1 relation.

For the sandwich model, it is

$$\begin{aligned}
 A_\lambda &= -2.5 \log_{10} \frac{I}{I_0} \\
 &= -2.5 \log_{10} \left(\frac{h_d}{h_s} \frac{1 - e^{-\tau_\lambda}}{\tau_\lambda} + \frac{1}{2} \left(1 - \frac{h_d}{h_s}\right) e^{-\tau_\lambda} + \frac{1}{2} \left(1 - \frac{h_d}{h_s}\right) \right), \quad (\text{C.5})
 \end{aligned}$$

where h_s is the thickness of the source layer and $h_d \leq h_s$ is that of a dust layer internal to the source one and sharing the same mid-plane: the solution is the combination of a slab model, of the dust-free portion of sources on the side opposite to the viewer attenuated by the dust screen, and of the unattenuated symmetric portion on the side of the viewer (the first, second and third terms of the logarithm in Eq. C.5, respectively; the sandwich is equivalent to the slab for $h_d = h_s$). As for the slab, $A_{V,BD}$ is the same as A_V in the optically thin limit. Instead, it goes to zero as $1/\tau_V$ at high A_V . The case for $h_d = h_s/2$ is shown in Fig. C.1.

For the slab and sandwich models we also made full radiative transfer calculation including scattering: we used the TRADING code (Bianchi 2008), assuming $h_d = h_s/2$ and albedos from the THEMIS model [$\omega(H\alpha) = 0.56$, $\omega(H\beta) = 0.52$]; and strong forward scattering, with an asymmetry parameter characteristic for MW dust, $g = 0.7$, at both wavelengths (Hensley & Draine 2021). We run 19 models with face-on optical depth τ_V between 0.1 and 20.

Results from radiative transfer calculations are also shown in Fig. C.1. The trends are qualitatively similar to the no-scattering cases, but with differences between $A_{V,BD}$ and A_V also in the optically thin limit. The full radiative transfer results for the slab and sandwich models are also discussed in Sect. 3.5 and plotted in Fig. 7.